Inhibition of p38-MK2 pathway enhances the efficacy of microtubule inhibitors in breast cancer cells

Yu-Chia Chen[1, 2, 7], Mamoru Takada[3, 7], Aerica Nagornyuk[4], Muhan Yu[1, 3], Hideyuki Yamada[3], Takeshi Nagashima[3], Masayuki Ohtsuka[3], Jennifer G. DeLuca[5], Steven M. Markus[5], Motoki Takaku[4], & Aussie Suzuki[1, 2, 6, 8]

1. McArdle Laboratory for Cancer Research, Department of Oncology, University of Wisconsin-Madison, Madison, Wisconsin, USA
2. Molecular Cellular Pharmacology Graduate Program, University of Wisconsin-Madison, Madison, Wisconsin, USA
3. Department of General Surgery, Graduate School of Medicine, Chiba University, Chiba, Japan
4. Department of Biomedical Science, University of North Dakota School of Medicine and Health Science, Grand Folks, North Dakota, USA
5. Department of Biochemistry and Molecular Biology, Colorado State University, Fort Collins, Colorado, USA
6. Carbone Comprehensive Cancer Center, University of Wisconsin-Madison, Madison, Wisconsin, USA
7. These authors contributed equally
8. Corresponding (aussie.suzuki@wisc.edu)

Competing Interest Statement: The authors declare no potential conflicts of interest.

Abstract

Microtubule-targeting agents (MTAs) have been successfully translated from basic research into clinical therapies and have been widely used as first- and second-line chemotherapy drugs for various cancers. However, current MTAs exhibit positive responses only in subsets of patients and are often accompanied by side effects due to their impact on normal cells. This underscores an urgent need to develop novel therapeutic strategies that enhance MTA efficacy while minimizing toxicity to normal tissues. In this study, we demonstrate that inhibition of the p38-MK2 (MAP kinase-activated protein kinase 2) pathway sensitizes cancer cells to MTA treatment. We utilize CMPD1, a dual-target inhibitor, to concurrently suppress the p38-MK2 pathway and microtubule dynamicity. In addition to its established role as an MK2 inhibitor, we find that CMPD1 rapidly induces microtubule depolymerization, preferentially at the microtubule plus-end, leading to the inhibition of tumor growth and cancer cell invasion in both *in vitro* and *in vivo* models. Notably, 10 nM CMPD1 is sufficient to induce irreversible mitotic defects in cancer cells, but not in non-transformed normal cells, highlighting its high specificity to cancer cells. We further validate that a specific p38-MK2 inhibitor significantly potentiates the efficacy of sub-clinical concentrations of MTA. In summary, our findings suggest that the p38-MK2 pathway presents a promising therapeutic target in combination with MTAs in cancer treatment.

Introduction

Cancer, a disease characterized by uncontrolled cell growth, results from cells that proliferate indefinitely without external growth signals[1,2]. Consequently, targeting cell cycle progression is a powerful therapeutic strategy for cancer treatment[3,4]. Microtubule-targeting agents (MTAs) disrupt spindle microtubule assembly during mitosis, making them widely-used chemotherapy drugs for various tumors[5-7]. By impairing microtubule dynamics and functions, MTAs activate the spindle assembly checkpoint (SAC)[8-10], leading to mitotic arrest, mitotic defects, and apoptotic cell death[5,11]. MTAs are functionally categorized into two groups: microtubule stabilizers (e.g., taxanes)[12,13] and microtubule depolymerizers (e.g., eribulin)[14,15]. Paclitaxel (PTX), a taxane, has been a highly successful anti-cancer drug in clinical use for over 30 years[12,16]. However, several limitations hinder its therapeutic efficacy. Firstly, only a subset of breast and ovarian cancer patients exhibit a favorable response to PTX[17-19]. Secondly, PTX lacks tumor specificity, leading to off-target effects, including neutropenia, gastrointestinal disorders, and peripheral neuropathy[20-24]. Thirdly, cancer cells can acquire resistance to PTX through mechanisms such as the upregulation of drug efflux proteins (e.g., P-glycoprotein) or class III β-tubulin, which reduces PTX binding affinity[25-27]. In contrast, eribulin, a second-line chemotherapeutic agent, has a lower incidence of peripheral neuropathy, one of the most troublesome side effect of MTAs[28]. Due to its distinct mechanism of action, eribulin is effective against taxane-resistant tumors[29-32]. However, clinical studies have demonstrated that fewer than 20% of metastatic breast cancer patients,

81 previously treated with chemotherapy, respond positively to eribulin[33,34]. MTAs remain
82 central to the treatment of breast and ovarian cancers, including metastatic cases. Therefore,
83 developing new strategies to overcome the limitations associated with MTAs is critical for
84 optimizing therapeutic outcomes in cancer treatment.

85 The p38 mitogen-activated protein kinase (MAPK) signaling pathway, activated by
86 a variety of environmental and intracellular stimuli[35-38], plays a crucial role in numerous
87 biological processes, including DNA repair, inflammation, cell differentiation, and cell death[39-
88 44]. MAPK-activated protein kinase 2 (MK2) is a major downstream substrate of p38 MAPK[45].
89 Previous studies have shown that phosphorylated MK2 localizes to mitotic spindles, and that
90 MK2 depletion leads to abnormal spindle formation, defects in chromosome alignment, and
91 mitotic arrest in both human cells and mouse oocytes, indicating a vital role of MK2 in mitotic
92 progression[46,47]. CMPD1 was originally developed as a selective inhibitor targeting the p38-
93 dependent phosphorylation of MK2 (**Fig. 1A**)[48-51]. Subsequent studies revealed that CMPD1
94 could induce G2/M arrest in glioblastoma and gastric cancer cells, as observed by flow
95 cytometry[52,53], and suggested its potential role in inhibiting microtubule polymerization *in*
96 *vitro*[53]. However, the precise and dynamic nature of CMPD1's effects on microtubule
97 dynamics and cancer cell proliferation have yet to be fully elucidated. In this study, we
98 demonstrate that CMPD1 preferentially induces severe mitotic defects in breast cancer cells
99 and effectively inhibits cancer cell growth, migration, and invasion in both *in vitro* and *in vivo*
100 models. Notably, CMPD1 uniquely triggers rapid microtubule depolymerization at the plus-

end *in vitro*. These results indicate that the inhibition of p38-MK2 pathway could enhance the therapeutic efficacy of MTAs. We validate this hypothesis by demonstrating that a specific MK2 inhibitor, MK2-IN-3, in combination with vinblastine, a clinically approved microtubule destabilizer[54,55], exhibits significantly increased efficacy in inducing mitotic defects. Thus, our results suggest that the p38-MK2 pathway may serve as a promising therapeutic target in combination with MTAs in cancer treatment.

Results

CMPD1 induces robust prometaphase arrest in breast cancer cell lines

Cell cycle inhibitors, particularly MTAs, are standard chemotherapy drugs for breast cancer[54]. To investigate whether CMPD1 induces G2/M arrest in breast cancer cells, we treated MDA-MB-231 cells, a triple-negative breast cancer (TNBC) cell line, with varying concentrations of CMPD1 and analyzed its effects on cell cycle progression using flow cytometry. The results demonstrated that CMPD1 effectively arrested MDA-MB-231 cells in the G2/M phase at concentrations ranging from 1 to 10 μM (**Fig. 1B**), consistent with previous observations in glioblastoma cells[53]. Given that flow cytometry is unable to distinguish between G2 phase and mitosis, we performed high-temporal resolution live-cell imaging to further dissect the impact of CMPD1 on cell cycle progression across various breast cancer cell lines, including MDA-MB-231 (TNBC), CAL-51 (TNBC), and T-47D (luminal A)[56,57]. Our findings revealed that CMPD1 induced a severe prometaphase arrest

121 across all tested breast cancer cell lines, regardless of subtypes, with most cells remaining
122 arrested in prometaphase for over 10 hours, while control cells divided within 30-60 min (**Fig.**
123 **1C-D** and **Supplementary Movies 1-2**). Since CAL-51 cells harbor wild-type TP53,
124 whereas the other two cell lines do not[58,59], these results suggest that CMPD1 induces a
125 robust prometaphase arrest in breast cancer cells through a p53-independent mechanism.
126

127 **Breast cancer cells exhibit heightened sensitivity to CMPD1 treatment compared to**
128 **normal cells.**

129 We demonstrated that concentrations exceeding 1 μM of CMPD1 effectively
130 induced a robust prometaphase arrest in multiple breast cancer cell lines (**Fig. 1D**). In
131 contrast, recent studies on MTA treatment for breast cancer have identified that the clinically
132 relevant concentration of PTX in tissue culture cells ranges from 5 to 50 nM[60]. Within this
133 range of concentration, PTX does not induce severe mitotic arrest as observed at higher
134 concentrations (> 1 μM), but it significantly increases the incidence of mitotic errors, thereby
135 promoting chromosomal instability (CIN) and ultimately leading to cancer cell death[60]. Given
136 these findings, we next explored whether sub-μM concentrations of CMPD1 could induce
137 CIN in breast cancer cells. To this end, we treated MDA-MB-231 and CAL-51 cells, along
138 with two non-transformed cell lines (breast epithelial MCF10A and retinal pigment epithelial
139 RPE1 cells), which served as a normal cell control, with either 10 or 50 nM CMPD1. We then
140 compared the impact of CMPD1 on chromosome segregation using live-cell imaging. In the

141 absence of CMPD1, no significant differences in mitotic duration were observed among
142 MCF10A, RPE1, MDA-MB-231, and CAL-51 cells (**Fig. 2A-C and Fig.2-Supplement 1A-**
143 **C**). However, upon treatment with 10 or 50 nM CMPD1, all cell lines were arrested in
144 prometaphase, except for MCF10A (**Fig. 2A-C**). Notably, MDA-MB-231 and CAL-51 cells
145 displayed significantly prolonged mitotic duration compared to MCF10A and RPE1 cells (**Fig.**
146 **2A-C and Fig.2-Supplement 1A-C**), indicating greater sensitivity of breast cancer cells to
147 CMPD1 treatment relative to normal cells. Given that mitotic errors are a direct cause of CIN,
148 we next assessed the frequency of mitotic errors including misaligned chromosome,
149 chromosome bridge, lagging chromosome, and multipolar division under these conditions
150 (**Fig. 2D**). Both MDA-MB-231 and CAL-51 cells exhibited a significantly higher rate of mitotic
151 errors when exposed to 10 or 50 nM CMPD1 (**Fig. 2E**). For instance, approximately 90%
152 and 100% of CAL-51 cells experienced mitotic errors in the presence of 10 and 50 nM
153 CMPD1, respectively (**Fig. 2E**). Conversely, 90~100% of MCF10A and RPE1 cells
154 underwent faithful cell division even at the same concentrations of CMPD1 (**Fig. 2E and**
155 **Fig.2-Supplement 1A-C**). To determine whether CMPD1 selectively targets cancer cells
156 compared to other MTAs, we evaluated mitotic error rates in the same cell lines treated with
157 a clinically relevant concentration of PTX (10 nM). Our results demonstrated that both RPE1
158 and breast cancer cell lines displayed comparably high rates of mitotic errors when treated
159 with 10 nM PTX treatment (**Fig. 2F**), consistent with previous observations[60]. In summary,
160 unlike PTX, CMPD1 induces CIN with selective toxicity toward breast cancer cells.

161 To further investigate the selectivity of CMPD1 in breast cancer cells, we conducted
162 a CMPD1 washout assay using the above cell lines, aiming to recapitulate the clinical
163 condition where the concentration of chemotherapy drugs in patients is diluted due to the
164 "drug holiday" between regular treatments. In this assay, we treated the cells with 2 μM
165 CMPD1 for 12 hours, followed by a washout before imaging. We observed that the mitotic
166 duration was significantly prolonged in both MDA-MB-231 and CAL-51 cells upon CMPD1
167 washout (85 min and 151 min, respectively) compared to RPE1 cells (14 min) (**Fig. 2G-H**
168 **and Fig. 2-Supplement 2A-B**). This suggests that breast cancer cells struggle to recover
169 from CMPD1-induced mitotic arrest, whereas normal cells can immediately resume
170 progression to proper anaphase. Notably, 90% and 81% of mitotic cells in MDA-MB-231 and
171 CAL-51 cells lines, respectively, exhibited mitotic errors, whereas 50% of RPE1 cells
172 displayed normal chromosome segregation (**Fig. 2G, I**). These findings reinforce the
173 hypothesis that breast cancer cells are more sensitive to CMPD1 treatment under clinically
174 relevant conditions. Interestingly, approximately 60% of MDA-MB-231 cells that entered
175 mitosis after CMPD1 washout still exhibited mitotic errors, while only ~10% of RPE1 cells
176 showed errors. This suggests a prolonged impact of CMPD1 on mitosis in breast cancer
177 cells (**Fig. 2-Supplement 2C**). Consistent with the increased sensitivity in breast cancer
178 cells to CMPD1, MDA-MB-231 cells exhibited a significantly higher frequency of apoptotic
179 cell death during or shortly after mitosis within 24 of CMPD1 washout, compared to RPE1
180 cells (**Fig. 2-Supplement 2D-E**).

181 To further validate the heightened sensitivity of breast cancer cells to CMPD1, we
182 measured its IC_{50} in MDA-MB-231, CAL-51, and MCF10A cells. Consistent with our live-cell
183 imaging results, both MDA-MB-231 and CAL-51 cells exhibited significantly lower IC_{50} (0.21
184 μM and 0.74 μM, respectively), compared to MCF10A cells (1.16 μM) (**Fig. 2-Supplement**
185 **3A-C**). Moreover, IC_{50} of p53 knockout CAL-51 cells[61] (0.88 μM) was comparable to that of
186 wild-type CAL-51 cells (0.74 μM) (**Fig. 2-Supplement 3D**), further supporting the notion that
187 CMPD1 induces a robust prometaphase arrest in breast cancer cells via a p53-independent
188 mechanism. Collectively, these results underscore that breast cancer cells are more
189 sensitive to CMPD1 treatment than normal MCF10A and RPE1 cells, particularly in a
190 clinically relevant context.
191

192 **CMPD1 inhibits anchorage independent growth and tumor growth in mouse**
193 **xenograft**

194 We subsequently evaluated the efficacy of CMPD1 in inhibiting anchorage-
195 independent growth, a critical hallmark of tumorigenesis, in MDA-MB-231 cells. CMPD1
196 demonstrated a potent dose-dependent inhibition, with 500 nM being sufficient to completely
197 suppress colony formation (**Fig. 3A-B and Fig. 3-Supplement 1A-B**). Remarkably, even at
198 a relatively lower concentration (250 nM), CMPD1 significantly reduced colony formation,
199 surpassing the inhibitory effects of 10 μM PTX. These findings suggest that CMPD1 is more
200 effective than PTX in inhibiting the anchorage-independent growth of MDA-MB-231 cells.

201 We demonstrated that CMPD1 effectively inhibits cancer cell growth in a tissue
202 culture model. Next, we investigated whether CMPD1 could also inhibit tumor growth *in vivo*.
203 To this end, we employed MDA-MB-231 and CAL-51 xenograft mouse models and found
204 that CMPD1 significantly suppressed the tumor growth (**Fig. 3C-G and Fig. 3-Supplement**
205 **1C-D**). Notably, while both PTX and CMPD1 suppressed tumor growth in mice, CMPD1
206 achieved comparable efficacy at concentrations 10-100 times lower than PTX (**Fig. 3D-G).**
207 Furthermore, mice in the CMPD1 treatment group continued to gain weight during the entire
208 treatment regimen, comparable to the control group (vehicle-treated mice), with no observed
209 mortality (**Fig. 3-Supplement 2A-B**). In contrast, the PTX-treated group exhibited a
210 significant reduction in body weight and an increased number of deaths of individuals (**Fig.**
211 **3-Supplement 2A-B**). Additionally, anatomical examination showed no apparent
212 abnormalities in kidneys or livers of CMPD1-treated mice, and blood marker analysis
213 confirmed no significant impairment in these organ functions in CMPD1-treated mice
214 compared to control (**Fig. 3-Supplement 3A-B**) Notably, the numbers of white blood cells
215 (WBC) were comparable between CMPD1-treated and control groups, while PTX-treated
216 group showed a marked decrease in WBC levels (**Fig. 3-Supplement 3C-D**). These findings
217 suggest that CMPD1 is not only effective in inhibiting tumor growth in both *in vitro* and *in vivo*
218 models but also appears to be more potent and safer than PTX, a standard
219 chemotherapeutic agent for breast cancer treatment.
220

221 **CMPD1 exhibits a preferential depolymerizing effect on the microtubule plus-end**

222 We demonstrated that at least ≥1 μM CMPD1 induced a robust prometaphase
223 arrest in breast cancer cell lines (**Fig. 1D**). A previous study suggests that CMPD1 may
224 possess the ability to inhibit tubulin polymerization, as indicated by *in vitro* tubulin
225 polymerization assay[53]. To elucidate the mechanism underlying the CMPD1-induced
226 prometaphase arrest, we performed high spatiotemporal resolution live-cell imaging to
227 monitor microtubule dynamics in metaphase CAL-51 cells (see **Methods**). In these cells, α-
228 tubulin and histone H2B genes were endogenously labeled with mNeonGreen and mScarlet,
229 respectively, using CRISPR-Cas9 technology[60]. Our results revealed that the signal intensity
230 of mitotic spindles dramatically decreased to less than 10% within 8 min following CMPD1
231 treatment (**Fig. 4A-B** and **Supplementary Movies 3-4**). Concurrently, the formation of
232 multipolar spindle poles was observed (**Fig. 4A**). The decrease in spindle signal intensity
233 correlated with a gradual disruption of the metaphase plate, likely due to the loss of
234 kinetochore-microtubule attachments (**Fig. 4A**). Moreover, we observed that CMPD1-
235 treated cells exited G2 phase and underwent nuclear envelope breakdown (NEBD), even
236 though these cells were unable to assemble mitotic spindles (**Fig. 4C**). This finding further
237 supports that CMPD1 specifically arrests cells in prometaphase rather than G2 phase. To
238 determine whether CMPD1 induces rapid microtubule depolymerization or the degradation
239 of tubulin proteins, we pre-treated the cells with MG132, a proteasome inhibitor, for 1 hour
240 prior to CMPD1 treatment (**Fig. 4A-B** and **Supplementary movie 5**). We found that

241 proteasome inhibition did not prevent the CMPD1-mediated reduction in spindle signals (**Fig.**
242 **4A-B**), suggesting that CMPD1 directly induces microtubule depolymerization in breast
243 cancer cells.

244 To further investigate the mechanism underlying CMPD1-induced microtubule
245 depolymerization, we conducted TIRFM (Total Internal Reflection Fluorescence Microscopy)
246 experiments to observe microtubule behaviors in response to CMPD1 treatment. The
247 conventional TIRFM assay utilizing PTX-stabilized immobilized microtubules is widely used
248 due to its ease of use. However, this approach lacks the dynamic nature of microtubules as
249 seen in living cells, limiting the study of CMPD1's effects under more physiological conditions.
250 To overcome this limitation, we utilized GMPCPP-stabilized microtubule seeds combined
251 with rhodamine-labeled tubulin, which allows for the observation of microtubule growth and
252 shrinkage at both ends, thereby better mimicking the dynamic behavior of microtubules in
253 mitotic cells. As expected, microtubules exhibited repeated cycles of growth and shrinkage
254 at both plus and minus ends, with a higher stability at minus ends (**Fig. 4D**). Upon treatment
255 with CMPD1, there was a marked reduction in the proportion of microtubules with plus-end
256 extensions within just 1 min (**Fig. 4D-F**), along with an increased frequency of microtubule
257 catastrophes, reduced growth rates, and decreased maximum lengths of plus-end
258 extensions (**Fig. 4G-H**). Interestingly, CMPD1's effects on the minus ends of microtubules
259 were notably different. Neither the fraction of microtubules with minus end extensions nor
260 the catastrophe frequency at minus ends were significantly different from control (**Fig. 4D-**

261 **H**). However, minor reductions were observed in the average maximum length of minus-end
262 extensions and their growth rates (**Fig. 4H**). In contrast, vinblastine, a well-characterized
263 microtubule destabilizer, rapidly depolymerized microtubules from both ends (**Fig. 4D-E**),
264 highlighting that CMPD1 uniquely and preferentially depolymerizes microtubules from the
265 plus ends. Collectively, our cell biology and biochemical data demonstrate that CMPD1
266 alone can depolymerize microtubules, with a pronounced preference for plus-end
267 depolymerization.
268

269 **CMPD1 inhibits cell migration and invasion**

270 Since proper microtubule dynamics is essential for regulating cell locomotion[62-64],
271 we hypothesized that the improper microtubule dynamics induced by CMPD1 might inhibit
272 cell migration. To investigate this, we evaluated the migratory capacity of CAL-51 cells using
273 a wound healing assay following treatment with CMPD1. Our findings revealed that CMPD1,
274 at concentrations ranging from 100 nM to 10 μM, significantly inhibited wound closure
275 compared to the DMSO-treated control (**Fig. 5A-B**), demonstrating its potential to suppress
276 cancer cell migration and invasion. To further examine this hypothesis, we conducted a
277 transwell-invasion assay using MDA-MB-231 cells. Treatment with CMPD1 at
278 concentrations greater than 100 nM significantly suppressed breast cancer cell invasion,
279 and at 1 μM, CMPD1 completely abolished this cancer invasion (**Fig. 5C-D**).

280 To determine whether CMPD1 inhibits cancer cell invasion *in vivo*, we assessed the

281 frequency of invasion of cancer cells into blood vessels by examining the tissue sections of
282 mice with cancer cell-derived xenografts described in **Fig. 3C**. CMPD1-treated mice
283 displayed a significantly reduced frequency of cancer cell-infiltrated vessels compared to
284 vehicle-treated mice, suggesting that CMPD1 significantly inhibits metastasis *in vivo* (**Fig.**
285 **5E**). Together, these results show that CMPD1 suppresses cancer cell migration and
286 invasion *in vitro* and *in vivo*.
287

288 **Inhibiting the p38-MK2 pathway significantly enhances the efficacy of microtubule**
289 **depolymerizing agents**

290 CMPD1's distinct capacity to inhibit tumor growth may stem from its dual inhibitory
291 effects on both the p38-MK2 signaling pathway and microtubule dynamics. To rigorously test
292 the hypothesis that inhibition of the p38-MK2 pathway could potentiate the efficacy of MTAs,
293 we assessed the combinatorial effects of MK2-IN-3 (hereafter referred to as MK2i), a
294 selective MK2 inhibitor[65], and vinblastine at clinically relevant concentrations (1 or 5 nM) on
295 mitotic progression in CAL-51 cells. We first confirmed that MK2i effectively inhibits MK2
296 activity in CAL-51 cells, as both 1 and 10 μM concentrations significantly reduced
297 phosphorylation levels of Hsp27, a key downstream phosphorylation substrate of MK2[66,67],
298 following H_2O_2-induced oxidative stress (**Fig. 6-Supplement 1A-B**). In contrast, treatment
299 with 10 μM Mk2i alone had no detectable impact on cell proliferation of CAL-51 cells over a
300 4-day period (**Fig. 6-Supplement 1C**). Consistent with these findings, treatment with either

301 10 μM MK2i or 1 nM vinblastine alone did not significantly alter the frequency of mitotic
302 slippage or mitotic cell death compared to the control (**Fig. 6A**). However, both individual
303 treatments modestly prolonged mitotic duration and increased the frequency of mitotic errors
304 (approximately 2 to 3-fold compared to control) (**Fig. 6A**). Strikingly, the combination of 10
305 μM MK2i with 1 nM vinblastine resulted in a profound synergistic effect, extending mitotic
306 duration by approximately 13-fold and markedly increasing the frequency of mitotic errors
307 and cell death (**Fig. 6A, Condition 4**). A similar synergistic effect was also observed when
308 cells were simultaneously treated with 10 μM MK2i and 5 nM vinblastine, although the 5 nM
309 vinblastine alone induced a more pronounced mitotic arrest compared to the control and 1
310 nM vinblastine (**Fig. 6A, Condition 6**). Importantly, similar synergistic effects, characterized
311 by elevated mitotic index and increased errors during metaphase and anaphase, were also
312 observed upon MK2 depletion by siRNA in cells treated with 1 nM vinblastine, further
313 reinforcing the notion that suppression of the MK2 signaling pathway can enhance MTA
314 efficacy (**Fig. 6-Supplement 2A-C**). To investigate whether this synergy extends beyond
315 mitosis, we next assessed the effects of MK2i and vinblastine co-treatment on TNBC cell
316 migration. As expected, both 10 μM MK2i and 1 nM vinblastine individually impaired cell
317 migration in CAL-51 cells, however, the combination treatment resulted in significantly
318 greater inhibition compared to individual treatment group or the control group (**Fig. 6-**
319 **Supplement 3A-B**).

320 To better understand the impact of CMPD1 treatment on cancer cells at the gene

321 expression level, we conducted RNA-seq analysis in MDA-MB-231 cells. When an FDR <
322 0.05 was applied using DESeq2 for differential gene expression analysis, 351 genes were
323 found to be up-regulated, and 425 genes were down-regulated 24 hours after treatment with
324 10 μM CMPD1 (**Fig. 6B, Fig. 6-Supplement Figure 4, and Fig. 6-Data file 1**). Gene
325 ontology (GO) biological process (BP) pathway enrichment analysis revealed that the most
326 significantly enriched pathways in up-regulated genes relate to cell migration, while down-
327 regulated genes are predominantly associated with mitosis and chromosome segregation
328 (**Fig. 6C and Fig. 6-Supplement Figure 4**). To explore whether unique pathways were up-
329 or down-regulated specifically in cancer cells, RNA-seq analysis was also performed on
330 RPE1 cells. Comparing differentially expressed genes between MDA-MB-231 cells and
331 RPE1 cells, cell death and apoptosis pathways were significantly enriched in genes uniquely
332 up-regulated in MDA-MB-231 cells (**Fig. 6D and Fig. 6-Data file 2**). Genes specifically
333 down-regulated in MDA-MB-231 cells were again enriched in pathways related to mitosis
334 and chromosome segregation (**Fig. 6D**), consistent to the results that cancer cells are more
335 sensitive to CMPD1 treatment (**Fig. 2**). Collectively, CMPD1 up-regulates cell death
336 pathways while selectively down-regulates mitotic genes in cancer cells, highlighting its
337 potent cancer cell specificity. The pivotal role of the p38-MK2 signaling pathway in enhancing
338 the efficacy of microtubule destabilizers likely contributes to these observed alterations in
339 gene expression.
340

341 **Discussion**

342 MTAs have been widely utilized as first- or second-line chemotherapy agents for
343 various cancer; however, MTA-based treatment is often compromised by several limitations,
344 including severe adverse effects and the development of drug resistance[20-24]. Consequently,
345 the development of novel therapeutic strategies to enhance the effectiveness of MTAs
346 remains critical for improving clinical outcomes in cancer patients. In this study, we propose
347 that inhibiting the p38-MK2 pathway can synergize with MTAs to significantly enhance their
348 therapeutic efficacy. We demonstrate this synergistic effect by using a combination of an
349 MK2-specific inhibitor with the microtubule depolymerizer vinblastine, alongside CMPD1, a
350 dual-target inhibitor that simultaneously disrupts both the MK2 signaling pathway and
351 microtubule dynamics (**Fig. 6A**). Our findings reveal that CMPD1 exhibits a unique ability to
352 depolymerize microtubules specifically at their plus-ends, as well as selectively inducing
353 mitotic defects and altering gene expression profiles in cancer cells (**Fig. 2, 4D-H,** and **6B-**
354 **D**). Furthermore, CMPD1 exhibited potency comparable to or greater than PTX in inhibiting
355 tumor growth both *in vitro* and *in vivo* (**Fig. 3**). In terms of tumor specificity, PTX at clinically
356 relevant concentrations lacks cancer selectivity[60], whereas CMPD1, at similar low
357 concentrations, specifically induces mitotic defects in breast cancer cells without affecting
358 mitotic fidelity in non-transformed cells (**Fig. 2**). These findings suggest that p38-MK2
359 inhibition has the potential to enhance MTA efficacy, allowing for the improved tumor growth
360 inhibition at a lower MTA concentration, thereby reducing the risk of side effects.

361 To gain a deeper understanding of CMPD1's cancer cell selectivity, we conducted
362 RNA-seq to compare global gene expression profiles between MDA-MB-231 and RPE1 cell
363 lines, both with or without CMPD1 treatment (**Fig. 6B**). CMPD1 treatment selectively up-
364 regulated gene pathways associated with cell death, aligning with its observed higher
365 cytotoxicity to cancer cells. The cancer-specific selectivity of CMPD1 may also be attributed
366 to differential expression levels of p38 and MK2. Previous studies have reported that MK2
367 is overexpressed in multiple myeloma (MM) and has a potential to serve as a marker of poor
368 prognosis[68,69]. Since MK2 facilitates the proliferation of MM cells by activating the Akt
369 signaling pathway, depletion or inhibition of MK2 significantly impairs the growth of MM
370 cells[68,69]. Furthermore, p38, MK2, and phospho-MK2 are markedly upregulated in primary
371 tumors of various cancers and exhibit an inverse correlation with overall survival rates[70-74].
372 Therefore, cancer cells with elevated MK2 or phospho-MK2 expression are likely more
373 sensitive to treatments involving MK2 inhibitors. However, further studies are required to
374 elucidate the detailed molecular mechanisms by which MK2 inhibitors enhance the efficacy
375 of MTAs. Our study has demonstrated synergistic effects between MK2 inhibitors and MTAs,
376 suggesting that the p38-MK2 pathway represents a promising therapeutic target in
377 combination with MTAs for cancer chemotherapy.
378
379
380

Acknowledgements

We thank Drs. Most S. Parvin, Ainslie Homan, Ozge Ali, Will Rossman, Terry Juang, Albert Wang, Masaharu Kasuya, Wang Junchao, Randy Owen, and Alex Li for help with data and image analysis. CAL-51 and CAL-51 p53 KO cells were kindly gifted from Drs. Beth Weaver, Mark Burkard, and Jennifer A. Pietenpol. Part of this work was supported by Wisconsin Partnership Program, Research Forward from the Office of the Vice Chancellor for Research (OVCR) and Wisconsin Alumni Research Foundation (WARF), start-up funding from University of Wisconsin-Madison SMPH, UW Carbone Cancer Center, and McArdle Laboratory for Cancer Research, and NIH grant R35GM147525 and U54AI170660 (to A.S.), NIH P20GM104360 and UND School of Medicine & Health Sciences Dean's fund (to M. Takaku), JSPS KAKENHI 21K08638 (to M. Takada), R35GM130365 and NSF NSF1518083 (to J. G. DeLuca), and R35GM139483 and NSF1518083 (to S. Markus).

Author Contributions: Y. Chen. performed most *in vitro* cell biology experiments and data analysis with guidance by A. Suzuki. M. Takada, M. Yu, H. Yamada, T. Nagashima, and M. Ohtsuka performed FACS, part of anchorage independent growth assay, mouse xenograft experiments, invasion assay, blood Invasion evaluation and related data analysis. M. Takada, A. Nagornyuk. and M. Takaku performed RNAseq experiments and data analysis. J. G. DeLuca and S.M. Markus performed in vitro microtubule dynamics experiments and data

401 analysis. A. Suzuki conceptualized and supervised the entire project. M. Suzuki and Y. Chen
402 drafted the manuscript, and M. Takada, S.M. Markus, J. G. DeLuca, and M. Takaku edited
403 manuscript. All authors revised and contributed to the manuscript.
404

405 **Materials and Methods**

406 **Cell Culture**

407 RPE1, MCF10A, CAL-51, MDA-MB-231, T47-D, and HeLa cells were originally obtained
408 from ATCC. These cells were grown in Dulbecco's modified Eagle's medium (DMEM; Gibco),
409 DMEM/F12 (Gibco), Mammary Epithelial Cell Growth Medium (MEBM: Lonza) with MEGM
410 kit (CC-4136, Lonza) and 100 ng/ml cholera toxin (Sigma, C8052), supplemented with 10%
411 FBS (Sigma), 100U/ml penicillin and 100 mg/ml streptomycin (Gibco) at 37 ˚C in a humid
412 atmosphere with 5% CO_2. CMPD1 (Abcam), Taxol (Sigma), MG132 (Sigma), and MPS1
413 inhibitor (SIGMA, AZ3146) were dissolved in DMSO (Sigma). For washout assay, cells were
414 incubated with 2 μM CMPD1 for 4 hours, then washed by pre-warmed complete media for
415 four times before starting live cell imaging. For the siRNA experiment shown in Figure 6-
416 Supplement Figure 2, RNAiMAX (Invitrogen) and ON-TARGET plus SMART pool siRNA
417 targeting MK2 (a mixture of four siRNAs; Horizon Discovery) were used according to the
418 manufacturer's protocols[75].
419

420 **Imaging**

421 For time lapse image acquisition, 3D stacked images were obtained sequentially with 1 μm
422 or 3 μm z steps for 12~15 μm total to cover entire mitotic cells using Nikon Elements software
423 and a high-resolution Nikon Ti-2 inverted microscope equipped with a high-resolution
424 Hamamatsu Flash V2 CMOS camera. The following objectives were used with above scope;
425 20x (NA 0.75 air), 40x (NA 1.25 silicon, for microtubule depolymerization in a cell), 60x (NA
426 1.4 oil), 100x (NA 1.4 oil). Images were takes by every 2 or 3 min interval for 24~72 hrs.
427 Cells were grown on glass bottom dish with #1.5 coverslips and incubated in a Tokai Hit STX
428 stage top incubator with PureBox Shiraito clean box (Tokai Hit). Feed-back control of Tokai
429 Hit stage top incubator was used to stably maintain 37 ˚C at growth medium. All imaging
430 was replicated at least three times. For fixed immunofluorescence experiments, cells were
431 grown on high-precision #1.5 coverslips and imaged by a Nikon Ti-2 equipped with a
432 Yokogawa SCU-W1-SoRa spinning disc confocal, Uniformizer, and a Hamamatsu Flash V3
433 CMOS camera. Quantitative image analysis was performed with Nikon Element (Nikon),
434 MetaMorph (Molecular Devices), and Imaris (Bitplane) (See details in Image analysis
435 section). No post-image processing was performed in all images. All imaging was replicated
436 at least two to four times.
437

438 **Image analysis**

439 Mitotic durations were measured time between NEBD and anaphase onset or
440 mitotic exit if cells did not exhibit anaphase onset such as CMPD1 treated cells. Histone

441 H2B-EGFP or -mScarlet/RFP was used for determination of mitotic stages. Those images
442 were analyzed using Nikon Element. Tubulin signal intensities on the spindle were measured
443 using intensities in the custom region of interest (ROI). ROI was drawn onto entire cells in
444 tubulin images, then additional ROI was drawn in cytoplasmic, which is avoided spindles.
445 Second ROI was used for background correction. Similar equation was used in our previous
446 study. Briefly, the integrated intensities from both ROIs were obtained, then the intensity of
447 second ROI was divided by area and times the area of entire cells (first ROI). This value was
448 used for corrections of background for the first ROI. For kinetochore signal measurement in
449 Figure 2B, Integrated fluorescence intensity (minus local background (BG)) measurements
450 were obtained for kinetochores as described previously[76]. A 13 x 13 pixel region was
451 centered on a fluorescent kinetochore to obtain integrated fluorescence, whereas a 15 x 15
452 pixel region centered on the 13 x 13 pixel region was used to obtain surrounding BG intensity.
453 Measured values were calculated by: Fi (integrated fluorescence intensity minus BG) =
454 integrated intensity for 13 x 13 region – (integrated intensity for the 15 x 15 – integrated
455 intensity for 13 x 13) x pixel area of the 13 x 13 / (pixel area of the 15 x 15 region – pixel area
456 of a 13 x 13 region). Measurements were made with Metamorph 7.7 software (Molecular
457 Devices) using Region Measurements[76]. At least two or three independent replicates of
458 measurements were performed. For cell migration and mobility analysis in Figure 5A-B, we
459 obtained the center of nucleus by particle detection module in Imaris software (Oxford
460 Instrument). The mobility or migration was tracked overtime and then the total length,

461 displacements, and speed were also obtained by Imaris software.

462

463 ***In vitro* microtubule dynamics assays**

464 Microtubules nucleated from GMPCPP-stabilized seeds were prepared and imaged as
465 follows. A microtubule seed mixture was assembled from 50 μM tubulin (7:1:2,
466 unlabeled:488-labeled: biotin-labeled) in BRB80 (80 mM PIPES, 1 mM $MgCl_2$, 1 mM EGTA,
467 pH 6.9), clarified by centrifugation at 90K rpm for 10 min, divided into 2 μl aliquots, snap-
468 frozen in liquid nitrogen, and stored at -80ºC. On the day of imaging, one of these aliquots
469 was thawed, and to this, 0.4 μl 10 mM GMPCPP (Jena Biosciences; 1 mM final) and 1.6 μl
470 BRB80 were added to bring the tubulin to a final concentration of 20 μM. The reaction was
471 incubated at 37ºC for 10 minutes (to promote polymerization) and stored at room
472 temperature for up to 1 day. To prepare for an imaging session, 1 μl of the polymerized
473 biotinylated-seed mixture was diluted 100X (to 200 nM final) into 79 μl BRB80 and 20 μl
474 0.75% methylcellulose (dissolved in BRB80), both at room temperature (the mixture was
475 pipetted up and down to sheer seeds into smaller sizes). Flow chambers (~4-6 μl in volume)
476 were assembled by adhering plasma-cleaned and biotin/PEGylated glass coverslips (as
477 described in a previous study[77]) to glass slides using double-stick tape. Streptavidin (0.1
478 mg/ml; in BRB80) was introduced into the imaging chamber, after which the chamber was
479 incubated at room temperature for 2-10 minutes. The chamber was washed with 10 μl
480 BRB80 supplemented with 1% Pluronic and incubated for ~10-30 seconds, after which 10

481 µl of the diluted biotinylated-seed mixture was introduced. The imaging chamber was then
482 immediately placed on a microscope stage prewarmed to 37ºC to monitor seed density in
483 the chamber (we did our best to ensure each chamber had a similar density of seeds).
484 Chambers were washed with 10 µl BRB80 supplemented with 1% Pluronic.

485 For the polymerization mix, a stock solution of 50 µM tubulin (12.5:1, unlabeled:
486 rhodamine-labeled tubulin) in BRB80 was prepared, clarified by centrifugation at 90K rpm
487 for 10 min, divided into 20 µl aliquots, snap frozen in liquid nitrogen, and stored at -80ºC.
488 Immediately prior to imaging, one of these aliquots was thawed and placed on ice. A 10 µl
489 polymerization mix (final tubulin concentration, 15 µM) was assembled using the following:
490 3 µl 50 µM tubulin (from above), 0.5 µl 20 mM GTP, 0.5 µl 20 mM β-mercaptoethanol, 2 µl
491 0.75% methylcellulose, 0.5 µl glucose oxidase/catalase mix (1.2 mg glucose oxidase + 28.1
492 µl catalase + 99.1 µl BRB80), 0.5 µl 30% glucose,1 µl casein (from a 5% stock of Alkali-
493 soluble Casein), and either 2 µL BRB80 or 2 µl of appropriate drug solution (20 µM CMPD1,
494 or 5 µM vinblastine, each of which was prepared in BRB80). Note that all reagents were
495 prepared or diluted in BRB80. The solution was gently mixed, warmed slightly between
496 gloved fingertips for 10-20 sec, and then immediately added to the flow chamber with the
497 adhered GMPCPP-stabilized microtubule seeds (as described above). Chambers were then
498 incubated for 15 minutes on the microscope state at 37ºC (to approach steady-state), after
499 which a freshly prepared polymerization mix with either tubulin only, or tubulin and a drug
500 was added to the chamber and imaged for 15-20 minutes. For experiments in which a drug

501 was added mid-way through the imaging period (see kymographs in Figure 4D), we did the
502 following: after the initial 15-minute incubation with tubulin only, a fresh polymerization mix
503 without drug was added, and a 20-minute movie was initiated. After 10 minutes, the movie
504 was briefly paused during which another freshly prepared polymerization mix with drug (or
505 tubulin only) was added to the chamber, and the acquisition was then continued.

506 Microtubule dynamics were imaged using total internal reflection fluorescence (TIRF)
507 microscopy on an inverted Nikon Ti-E using a 1.49 NA 100X objective equipped with a Ti-S-
508 E motorized stage (Nikon), piezo Z-control (Physik Instrumente), a motorized filter cube
509 turret, a stage-top incubation system (LiveCell, Pathology Devices), and an iXon X3 DU897
510 cooled EM-CCD camera (Andor). We used 488 nm and 561 nm lasers (Nikon), a multi-pass
511 quad filter cube set (C-TIRF for 405 nm/488 nm/561 nm/638 nm; Chroma), and emission
512 filters mounted in a filter wheel (525 nm/50 nm, 600 nm/50 nm; Chroma). Images were
513 acquired every 10 seconds. The microscope system was controlled by NIS-Elements
514 software (Nikon), and images were analyzed using FIJI/ImageJ (NIH). Microtubule plus and
515 minus ends were identified by exhibiting dynamics parameters distinct to each end (see
516 kymographs in Figure 4D for examples).

517

518 **Anchorage independent growth assay**

519 6-well dish (Eppendorf) was used for anchorage independent growth assay. 2ml of
520 autoclaved 1% agarose was used for bottom layer. After bottom layer became solid, 24 x

521 10^3 cells (MDA-MB-231 cells) were mixed into 2 ml of 0.8% agarose / media with or without
522 CMPD1 or Taxol. After top layer gel became solid, cells were incubated in a humid
523 atmosphere with 5% CO_2 for three weeks. 3 drops of complete media were supplied in each
524 well every 3 days to avoid drying out. Cells were stained by 100 μg/ml of iodonitrotetrazolium
525 chloride solution (Sigma) prior to taking photos.
526

527 **Wound healing assay**

528 H2B-mscarlet CAL-51 cells were plated in a 8-well chamber slide (ibidi, 80807). 24 hours
529 after cell seeding, a stripe of cell-free zone (the wound) was manually created on a highly
530 confluent monolayer of cells using a sterile pipette tip. The cell culture media was then
531 immediately replaced with a new one containing the indicated drugs (DMSO, 0.1, 0.5, 1, and
532 10 μM CMPD1). Then, the cell locomotion dynamics was monitored with live-cell imaging at
533 an interval of 30 min. To quantify the cell migration efficiency in each condition, we used an
534 ImageJ macro to measure the distance between two boundaries of the wound. Briefly, the
535 two boundaries of the wound were drawn and defined manually. Then, 40 lines
536 perpendicular to the two boundaries were drawn automatically and the length of each line
537 was calculated and shown. The distance of cell movement was calculated by subtracting
538 the distance at 20 hr post drug treatment from the original distance (0 hr). Each condition
539 was normalized to the control.
540

541 **Trans-well migration assay**

542 CytoSelect 24-well cell invasion assay kits (Cell Biolabs) or VitroGel Invasion assay kits
543 (TheWell Bioscience) utilizing basement membrane-coated inserts were used according to
544 the manufacturer's protocol. Following the overnight starvation of MDA-MB-231 or CAL-51
545 cells, the cells were seeded at 3.0 × 104 cells/well in the upper chamber and incubated with
546 the media containing DMSO (control), CMPD1, vinblastine, MK2i, or vinblastine plus MK2i
547 in the lower chamber for 24 or 48 hours. The invasive cells passing through the basement
548 membrane layer were stained, and the absorbance of each well was measured at 560 nm
549 after extraction.

550

551 **Blood Invasion evaluation**

552 All slides from mouse tumor with or without CMPD1 treatments were stained with HE and
553 were screened for vascular invasion using strict criteria based on previous reports [78,79]. All
554 slides were blindly evaluated by two investigators (MT and HY). All these vascular invasions
555 were adopted only if they were picked up on HE staining. Vascular invasion was identified
556 by tumor cells within vessels. The cases were categorized as blood vessel invasion-positive
557 or negative. Typical histologic pictures of blood vessel invasion positive and negative by HE
558 staining are shown in Figure 5E.

559

560 **RNA-seq**

561 24 hours after 10 μM CMPD1 treatment, RNAs were purified by the RNeasy Mini Kit
562 (Qiagen). For MDA-MB-231 cells, RNA-seq library preparation was conducted with the
563 QuantSeq 3' mRNA-Seq Library Prep Kit FWD for Illumina (LEXOGEN), and the libraries
564 were sequenced on a NextSeq500 at Kazusa DNA Research Institute. In the case of RPE1
565 cells, sequencing libraries were prepared using the TruSeq Stranded mRNA Kit and
566 sequenced on a NovaSeq 6000 at Macrogen Japan. Adapter sequences were removed from
567 the raw sequencing data, and after adapter trimming, reads were mapped to the human
568 reference genome (GRCh38) using the STAR aligner[80]. Read counts for each gene were
569 collected by featureCounts (version v1.6.4)[81]. Differentially expressed genes were identified
570 with DESeq2[82] using filtering thresholds of FDR < 0.05. Pathway enrichment analysis was
571 performed by DAVID[83].
572

573 **Tumor xenograft**

574 CB17-Prkdc^{scid}/Jcl mice were used for establishment of orthotopic breast cancer model and
575 therapy. This mice strain was purchased from CLEA Japan, Inc. (Tokyo, Japan). Mice were
576 maintained under specific pathogen-free conditions at the Chiba University. All experimental
577 procedures were performed in strict accordance with the National Institute of Health
578 guidelines and were approved by the Institutional Animal Care and Use Committee of Chiba
579 University. For in vivo experiments, samples sizes were determined on the basis of
580 knowledge of inter-tumor growth rate variability, gained from previous model-specific

experience. MDA-MB-231 and CAL- 51 cells (1×10^6 cells / 0.1 ml) in 1:1 PBS: Matrigel were subcutaneously injected into the mammary fat pad of female mice. The experiment was performed twice. The first experiment used MDA-MB-231 cells and the second experiment used both MDA-MB-231 and CAL-51 cells. In the first experiment, tumors were allowed to develop for 30 days, after which mice were randomly assigned to each treatment group, ensuring that baseline tumor volumes were balanced between treatment arms. The mice were treated with CMPD1 (i.p., 15 μg/mouse/injection, 10 times for 3 weeks) or PTX (i.p., 5 mg/kg/injection, 10 times for 3 weeks). In the second experiment, treatment was started on the 10th day after transplantation, and the treatment drug was administered five times over 16 days until the 26th day. During the second experiment, weight was measured, blood was collected at the end of the study, and the liver and kidneys were also removed for further analysis. Both maximum and minimum diameters of the resulting tumors were measured every other day using a slide caliper. Tumor volumes were calculated as previously described. Mice were euthanized via CO_2 inhalation. The maximum tumor diameter permitted under the relevant animal protocols is 25 mm, and this limit was not exceeded in any experiment.

Biochemical analysis of animal models

Whole blood samples were collected from all mice and blood biochemistry determinations were performed with an Automatic Analyzer Model 7070 (Hitachi Co., Ltd., Tokyo, Japan).

601 Parameters were aspartate aminotransferase (AST), alanine aminotransferase (ALT), γ-
602 glutamyl transpeptidase (GGT), blood urea nitrogen (BUN) and creatinine (CRE) (Oriental
603 Yeast Co., Ltd., Tokyo, Japan).
604
605 Hematoxylin and Eosin (HE) Staining
606 HE staining was performed using tissue samples obtained from the xenograft model. Tissue
607 samples were thin sliced to a thickness of 4 μm. For staining, slides were first stained with
608 hematoxylin for 5 minutes, followed by eosin staining for 2 minutes. The slides were then
609 dehydrated through a series of ethanol solutions, cleared in xylene, and mounted. The
610 staining was evaluated based on the tissue morphology.
611
612 Giemsa Staining
613 Slides were fixed in absolute methanol for 30 seconds to facilitate cell attachment and
614 preserve optimal staining characteristics, then allowed to air dry. The slides were immersed
615 in Wright-Giemsa stain (container 1) for 60 seconds without agitation. For the Rapid Wright's
616 One-Step Stain reagent, the staining duration was reduced to 15-30 seconds. Excess stain
617 was removed by draining or blotting the edges of the slides, avoiding direct contact with the
618 smear. The slides were then immersed in buffer solution (container 2) for 60 seconds (15-
619 45 seconds for the Rapid Wright's reagent), followed by draining to remove excess buffer.
620 Subsequently, the slides were dipped in rinse solution (container 3) for 2-10 seconds, with

621 the Rapid Wright's reagent requiring quick dips for 25 seconds. Excessive buffering and
622 rinsing were avoided to prevent decolorization. The slides were air-dried in a vertical position
623 on a paper towel. For microscopic analysis, leukocytes were counted per field at low
624 magnification, ensuring that fields were selected uniformly across specimens.
625
626 **FACS**
627 MDA-MB-231 cells were incubated with present or absent of CMPD1 for 24 hours. Cells
628 were then twice washed by PBS. Approximately 2 x 10^6 cells were fixed by ice cold Ethanol
629 for 16 hours. Samples were washed by cold PBS, and stained by PI (Sigma) containing
630 Triton-X (Sigma), and DNAse-free RNAse A (Sigma) in PBS for 30 min. Then samples were
631 measured by a flow cytometer.
632
633 **Statistics**
634 Statistical significance was determined using two tailed unpaired student's t-test for
635 comparison between two independent groups or one way ANOVA for multiped comparison.
636 Two-tailed T-test was performed for Fig. 1C, 1G, 2A-B, 4A-B, 4E, and supplementary figs
637 4A, 4E-F, 6B-C, 6E, 7C-E. One way ANOVA (multiple comparison) was performed for figs
638 1D, 2H-I, 3B, 3D, 3G, 4D, 5B, 5F-G, and Fig 3-Supplemen 2A. For TIRF experiments in
639 Figure 2 G-I, p values were calculated from Z scores (2G; as previously described in Marzo
640 et al., 2019; PMID 31364990), Mann–Whitney tests (2H-I, left and right), or by unpaired two-

641 tailed Welch's t-tests (2H-I, middle). The latter two tests were selected as follows: the
642 unpaired two-tailed Welch's t-test was used when the data sets were determined to be
643 normal (by the D'Agostino and Pearson test for normality; $p > 0.05$). In the case where only
644 one (or neither) was determined to be normal ($p < 0.05$), the Mann-Whitney test was used.
645 For significance, * $p < 0.05$, ** $p < 0.01$, *** $p < 0.001$, **** $p < 0.0001$ were considered
646 statistically significant. All quantifications were replicated at least two independent
647 experiments.

648

649 **Data availability**

650 RNA-seq data generated in this study are available at Gene Expression Omnibus under
651 Accession Number: GSE224462:
652 Go to https://www.ncbi.nlm.nih.gov/geo/query/acc.cgi?acc=GSE224462

653
654
655
656
657
658
659
660
661
662
663
664
665
666
667
668

669
670
671 ## References

672 1. Hanahan, D., and Weinberg, R.A. (2011). Hallmarks of cancer: the next generation. Cell *144*, 646-674.
673 10.1016/j.cell.2011.02.013.
674 2. Aaronson, S.A. (1991). Growth factors and cancer. Science *254*, 1146-1153. 10.1126/science.1659742.
675 3. Chan, K.S., Koh, C.G., and Li, H.Y. (2012). Mitosis-targeted anti-cancer therapies: where they stand. Cell Death Dis
676 *3*, e411. 10.1038/cddis.2012.148.
677 4. Manchado, E., Guillamot, M., and Malumbres, M. (2012). Killing cells by targeting mitosis. Cell Death Differ *19*,
678 369-377. 10.1038/cdd.2011.197.
679 5. Matson, D.R., and Stukenberg, P.T. (2011). Spindle poisons and cell fate: a tale of two pathways. Mol Interv *11*,
680 141-150. 10.1124/mi.11.2.12.
681 6. Tischer, J., and Gergely, F. (2019). Anti-mitotic therapies in cancer. J Cell Biol *218*, 10-11. 10.1083/jcb.201808077.
682 7. Mukhtar, E., Adhami, V.M., and Mukhtar, H. (2014). Targeting microtubules by natural agents for cancer therapy.
683 Mol Cancer Ther *13*, 275-284. 10.1158/1535-7163.MCT-13-0791.
684 8. Musacchio, A. (2015). The Molecular Biology of Spindle Assembly Checkpoint Signaling Dynamics. Current
685 biology : CB *25*, R1002-1018. 10.1016/j.cub.2015.08.051
686 S0960-9822(15)01045-3 [pii].
687 9. Lara-Gonzalez, P., Pines, J., and Desai, A. (2021). Spindle assembly checkpoint activation and silencing at
688 kinetochores. Semin Cell Dev Biol *117*, 86-98. 10.1016/j.semcdb.2021.06.009.
689 10. Musacchio, A., and Salmon, E.D. (2007). The spindle-assembly checkpoint in space and time. Nature reviews.
690 Molecular cell biology *8*, 379-393. nrm2163 [pii]
691 10.1038/nrm2163.
692 11. Jordan, M.A. (2002). Mechanism of action of antitumor drugs that interact with microtubules and tubulin. Curr
693 Med Chem Anticancer Agents *2*, 1-17. 10.2174/1568011023354290.
694 12. Weaver, B.A. (2014). How Taxol/paclitaxel kills cancer cells. Mol Biol Cell *25*, 2677-2681. 10.1091/mbc.E14-04-
695 0916.
696 13. Schiff, P.B., Fant, J., and Horwitz, S.B. (1979). Promotion of microtubule assembly in vitro by taxol. Nature *277*,
697 665-667. 10.1038/277665a0.
698 14. Perez, E.A. (2009). Microtubule inhibitors: Differentiating tubulin-inhibiting agents based on mechanisms of
699 action, clinical activity, and resistance. Mol Cancer Ther *8*, 2086-2095. 10.1158/1535-7163.MCT-09-0366.
700 15. Jordan, M.A., Kamath, K., Manna, T., Okouneva, T., Miller, H.P., Davis, C., Littlefield, B.A., and Wilson, L. (2005).
701 The primary antimitotic mechanism of action of the synthetic halichondrin E7389 is suppression of microtubule
702 growth. Mol Cancer Ther *4*, 1086-1095. 10.1158/1535-7163.MCT-04-0345.
703 16. Abu Samaan, T.M., Samec, M., Liskova, A., Kubatka, P., and Busselberg, D. (2019). Paclitaxel's Mechanistic and
704 Clinical Effects on Breast Cancer. Biomolecules *9*. 10.3390/biom9120789.
705 17. Fountzilas, G., Dafni, U., Dimopoulos, M.A., Koutras, A., Skarlos, D., Papakostas, P., Gogas, H., Bafaloukos, D.,
706 Kalogera-Fountzila, A., Samantas, E., et al. (2009). A randomized phase III study comparing three anthracycline-
707 free taxane-based regimens, as first line chemotherapy, in metastatic breast cancer: a Hellenic Cooperative
708 Oncology Group study. Breast Cancer Res Treat *115*, 87-99. 10.1007/s10549-008-0047-9.

709 18. Holmes, F.A., Walters, R.S., Theriault, R.L., Forman, A.D., Newton, L.K., Raber, M.N., Buzdar, A.U., Frye, D.K., and
710 Hortobagyi, G.N. (1991). Phase II trial of taxol, an active drug in the treatment of metastatic breast cancer. J Natl
711 Cancer Inst *83*, 1797-1805. 10.1093/jnci/83.24.1797-a.
712 19. Kohn, E.C., Sarosy, G., Bicher, A., Link, C., Christian, M., Steinberg, S.M., Rothenberg, M., Adamo, D.O., Davis, P.,
713 Ognibene, F.P., et al. (1994). Dose-Intense Taxol: High Response Rate in Patients With Platinum-Resistant
714 Recurrent Ovarian Cancer. JNCI Journal of the National Cancer Institute *86*, 18-24. 10.1093/jnci/86.1.18.
715 20. Brewer, J.R., Morrison, G., Dolan, M.E., and Fleming, G.F. (2016). Chemotherapy-induced peripheral neuropathy:
716 Current status and progress. Gynecol Oncol *140*, 176-183. 10.1016/j.ygyno.2015.11.011.
717 21. Armstrong, D.K., Bundy, B., Wenzel, L., Huang, H.Q., Baergen, R., Lele, S., Copeland, L.J., Walker, J.L., Burger, R.A.,
718 and Gynecologic Oncology, G. (2006). Intraperitoneal cisplatin and paclitaxel in ovarian cancer. N Engl J Med *354*,
719 34-43. 10.1056/NEJMoa052985.
720 22. Banerji, A., Lax, T., Guyer, A., Hurwitz, S., Camargo, C.A., Jr., and Long, A.A. (2014). Management of
721 hypersensitivity reactions to Carboplatin and Paclitaxel in an outpatient oncology infusion center: a 5-year review.
722 J Allergy Clin Immunol Pract *2*, 428-433. 10.1016/j.jaip.2014.04.010.
723 23. Lipton, R.B., Apfel, S.C., Dutcher, J.P., Rosenberg, R., Kaplan, J., Berger, A., Einzig, A.I., Wiernik, P., and Schaumburg,
724 H.H. (1989). Taxol produces a predominantly sensory neuropathy. Neurology *39*, 368-373. 10.1212/wnl.39.3.368.
725 24. Misawa, S., Denda, T., Kodama, S., Suzuki, T., Naito, Y., Kogawa, T., Takada, M., Suichi, T., Shiosakai, K., Kuwabara,
726 S., and Miro, C.I.P.s.g. (2023). Efficacy and safety of mirogabalin for chemotherapy-induced peripheral
727 neuropathy: a prospective single-arm trial (MiroCIP study). BMC Cancer *23*, 1098. 10.1186/s12885-023-11560-
728 4.
729 25. Kavallaris, M., Kuo, D.Y., Burkhart, C.A., Regl, D.L., Norris, M.D., Haber, M., and Horwitz, S.B. (1997). Taxol-resistant
730 epithelial ovarian tumors are associated with altered expression of specific beta-tubulin isotypes. J Clin Invest
731 *100*, 1282-1293. 10.1172/JCI119642.
732 26. Kavallaris, M. (2010). Microtubules and resistance to tubulin-binding agents. Nat Rev Cancer *10*, 194-204.
733 10.1038/nrc2803.
734 27. Seve, P., and Dumontet, C. (2008). Is class III beta-tubulin a predictive factor in patients receiving tubulin-binding
735 agents? Lancet Oncol *9*, 168-175. 10.1016/S1470-2045(08)70029-9.
736 28. Eslamian, G., Wilson, C., and Young, R.J. (2017). Efficacy of eribulin in breast cancer: a short report on the
737 emerging new data. Onco Targets Ther *10*, 773-779. 10.2147/OTT.S102638.
738 29. Smith, J.A., Wilson, L., Azarenko, O., Zhu, X., Lewis, B.M., Littlefield, B.A., and Jordan, M.A. (2010). Eribulin binds
739 at microtubule ends to a single site on tubulin to suppress dynamic instability. Biochemistry *49*, 1331-1337.
740 10.1021/bi901810u.
741 30. O'Shaughnessy, J., McIntyre, K., Schwartzberg, L., Wilks, S., Puhalla, S., Berrak, E., Song, J., and Vahdat, L. (2015).
742 Impact of prior anthracycline or taxane use on eribulin effectiveness as first-line treatment for metastatic breast
743 cancer: results from two phase 2, multicenter, single-arm studies. Springerplus *4*, 532. 10.1186/s40064-015-
744 1322-y.
745 31. Dumontet, C., and Jordan, M.A. (2010). Microtubule-binding agents: a dynamic field of cancer therapeutics. Nat
746 Rev Drug Discov *9*, 790-803. 10.1038/nrd3253.
747 32. Cortes, J., O'Shaughnessy, J., Loesch, D., Blum, J.L., Vahdat, L.T., Petrakova, K., Chollet, P., Manikas, A., Diéras, V.,
748 Delozier, T., et al. (2011). Eribulin monotherapy versus treatment of physician's choice in patients with metastatic

749 breast cancer (EMBRACE): a phase 3 open-label randomised study. The Lancet *377*, 914-923. 10.1016/s0140-
750 6736(11)60070-6.
751 33. Cortes, J., O'Shaughnessy, J., Loesch, D., Blum, J.L., Vahdat, L.T., Petrakova, K., Chollet, P., Manikas, A., Dieras, V.,
752 Delozier, T., et al. (2011). Eribulin monotherapy versus treatment of physician's choice in patients with metastatic
753 breast cancer (EMBRACE): a phase 3 open-label randomised study. Lancet *377*, 914-923. 10.1016/S0140-
754 6736(11)60070-6.
755 34. Cortes, J., Vahdat, L., Blum, J.L., Twelves, C., Campone, M., Roche, H., Bachelot, T., Awada, A., Paridaens, R.,
756 Goncalves, A., et al. (2010). Phase II study of the halichondrin B analog eribulin mesylate in patients with locally
757 advanced or metastatic breast cancer previously treated with an anthracycline, a taxane, and capecitabine. J Clin
758 Oncol *28*, 3922-3928. 10.1200/JCO.2009.25.8467.
759 35. Wood, C.D., Thornton, T.M., Sabio, G., Davis, R.A., and Rincon, M. (2009). Nuclear localization of p38 MAPK in
760 response to DNA damage. Int J Biol Sci *5*, 428-437. 10.7150/ijbs.5.428.
761 36. Borisova, M.E., Voigt, A., Tollenaere, M.A.X., Sahu, S.K., Juretschke, T., Kreim, N., Mailand, N., Choudhary, C.,
762 Bekker-Jensen, S., Akutsu, M., et al. (2018). p38-MK2 signaling axis regulates RNA metabolism after UV-light-
763 induced DNA damage. Nat Commun *9*, 1017. 10.1038/s41467-018-03417-3.
764 37. Yamashita, M., Fatyol, K., Jin, C., Wang, X., Liu, Z., and Zhang, Y.E. (2008). TRAF6 mediates Smad-independent
765 activation of JNK and p38 by TGF-beta. Mol Cell *31*, 918-924. 10.1016/j.molcel.2008.09.002.
766 38. Han, J., Lee, J.D., Bibbs, L., and Ulevitch, R.J. (1994). A MAP kinase targeted by endotoxin and hyperosmolarity in
767 mammalian cells. Science *265*, 808-811. 10.1126/science.7914033.
768 39. Colomer, C., Margalef, P., Villanueva, A., Vert, A., Pecharroman, I., Sole, L., Gonzalez-Farre, M., Alonso, J.,
769 Montagut, C., Martinez-Iniesta, M., et al. (2019). IKKalpha Kinase Regulates the DNA Damage Response and
770 Drives Chemo-resistance in Cancer. Mol Cell *75*, 669-682 e665. 10.1016/j.molcel.2019.05.036.
771 40. Arthur, J.S., and Ley, S.C. (2013). Mitogen-activated protein kinases in innate immunity. Nat Rev Immunol *13*,
772 679-692. 10.1038/nri3495.
773 41. Segales, J., Perdiguero, E., and Munoz-Canoves, P. (2016). Regulation of Muscle Stem Cell Functions: A Focus on
774 the p38 MAPK Signaling Pathway. Front Cell Dev Biol *4*, 91. 10.3389/fcell.2016.00091.
775 42. Canovas, B., and Nebreda, A.R. (2021). Diversity and versatility of p38 kinase signalling in health and disease. Nat
776 Rev Mol Cell Biol *22*, 346-366. 10.1038/s41580-020-00322-w.
777 43. Cuadrado, A., and Nebreda, A.R. (2010). Mechanisms and functions of p38 MAPK signalling. Biochem J *429*, 403-
778 417. 10.1042/BJ20100323.
779 44. Young, P.R. (2013). Perspective on the discovery and scientific impact of p38 MAP kinase. J Biomol Screen *18*,
780 1156-1163. 10.1177/1087057113497401.
781 45. Gurgis, F.M., Ziaziaris, W., and Munoz, L. (2014). Mitogen-activated protein kinase-activated protein kinase 2 in
782 neuroinflammation, heat shock protein 27 phosphorylation, and cell cycle: role and targeting. Mol Pharmacol
783 *85*, 345-356. 10.1124/mol.113.090365.
784 46. Yuan, J., Xu, B.Z., Qi, S.T., Tong, J.S., Wei, L., Li, M., Ouyang, Y.C., Hou, Y., Schatten, H., and Sun, Q.Y. (2010). MAPK-
785 activated protein kinase 2 is required for mouse meiotic spindle assembly and kinetochore-microtubule
786 attachment. PLoS One *5*, e11247. 10.1371/journal.pone.0011247.
787 47. Tang, J., Yang, X., and Liu, X. (2008). Phosphorylation of Plk1 at Ser326 regulates its functions during mitotic
788 progression. Oncogene *27*, 6635-6645. 10.1038/onc.2008.262.

789 48. Davidson, W., Frego, L., Peet, G.W., Kroe, R.R., Labadia, M.E., Lukas, S.M., Snow, R.J., Jakes, S., Grygon, C.A.,
790 Pargellis, C., and Werneburg, B.G. (2004). Discovery and characterization of a substrate selective p38alpha
791 inhibitor. Biochemistry *43*, 11658-11671. 10.1021/bi0495073.
792 49. Mamidi, P., Nayak, T.K., Kumar, A., Kumar, S., Chatterjee, S., De, S., Datey, A., Ghosh, S., Keshry, S.S., Singh, S., et
793 al. (2021). MK2a inhibitor CMPD1 abrogates chikungunya virus infection by modulating actin remodeling
794 pathway. PLoS Pathog *17*, e1009667. 10.1371/journal.ppat.1009667.
795 50. Wu, Y., He, H., Ding, Y., Liu, S., Zhang, D., Wang, J., Jiang, H., Zhang, D., Sun, L., Ye, R.D., and Qian, F. (2018). MK2
796 mediates macrophage activation and acute lung injury by regulating let-7e miRNA. Am J Physiol Lung Cell Mol
797 Physiol *315*, L371-L381. 10.1152/ajplung.00019.2018.
798 51. Hendriks, B.S., Seidl, K.M., and Chabot, J.R. (2010). Two additive mechanisms impair the differentiation of
799 'substrate-selective' p38 inhibitors from classical p38 inhibitors in vitro. BMC Syst Biol *4*, 23. 10.1186/1752-0509-
800 4-23.
801 52. Li, Y., Zhang, D., Yu, K., Hu, Y., Wu, Q., Qian, F., and Wang, Z. (2018). CMPD1 inhibited human gastric cancer cell
802 proliferation by inducing apoptosis and G2/M cell cycle arrest. Biol Res *51*, 11. 10.1186/s40659-018-0159-6.
803 53. Gurgis, F., Akerfeldt, M.C., Heng, B., Wong, C., Adams, S., Guillemin, G.J., Johns, T.G., Chircop, M., and Munoz, L.
804 (2015). Cytotoxic activity of the MK2 inhibitor CMPD1 in glioblastoma cells is independent of MK2. Cell Death
805 Discov *1*, 15028. 10.1038/cddiscovery.2015.28.
806 54. Jordan, M.A., and Wilson, L. (2004). Microtubules as a target for anticancer drugs. Nat Rev Cancer *4*, 253-265.
807 10.1038/nrc1317.
808 55. Moudi, M., Go, R., Yien, C.Y., and Nazre, M. (2013). Vinca alkaloids. Int J Prev Med *4*, 1231-1235.
809 56. Dai, X., Cheng, H., Bai, Z., and Li, J. (2017). Breast Cancer Cell Line Classification and Its Relevance with Breast
810 Tumor Subtyping. J Cancer *8*, 3131-3141. 10.7150/jca.18457.
811 57. Neve, R.M., Chin, K., Fridlyand, J., Yeh, J., Baehner, F.L., Fevr, T., Clark, L., Bayani, N., Coppe, J.P., Tong, F., et al.
812 (2006). A collection of breast cancer cell lines for the study of functionally distinct cancer subtypes. Cancer Cell
813 *10*, 515-527. 10.1016/j.ccr.2006.10.008.
814 58. Huovinen, M., Loikkanen, J., Myllynen, P., and Vahakangas, K.H. (2011). Characterization of human breast cancer
815 cell lines for the studies on p53 in chemical carcinogenesis. Toxicol In Vitro *25*, 1007-1017.
816 10.1016/j.tiv.2011.03.018.
817 59. Tentler, J.J., Ionkina, A.A., Tan, A.C., Newton, T.P., Pitts, T.M., Glogowska, M.J., Kabos, P., Sartorius, C.A., Sullivan,
818 K.D., Espinosa, J.M., et al. (2015). p53 Family Members Regulate Phenotypic Response to Aurora Kinase A
819 Inhibition in Triple-Negative Breast Cancer. Mol Cancer Ther *14*, 1117-1129. 10.1158/1535-7163.MCT-14-0538-
820 T.
821 60. Scribano, C.M., Wan, J., Esbona, K., Tucker, J.B., Lasek, A., Zhou, A.S., Zasadil, L.M., Molini, R., Fitzgerald, J., Lager,
822 A.M., et al. (2021). Chromosomal instability sensitizes patient breast tumors to multipolar divisions induced by
823 paclitaxel. Sci Transl Med *13*, eabd4811. 10.1126/scitranslmed.abd4811.
824 61. Redman-Rivera, L.N., Shaver, T.M., Jin, H., Marshall, C.B., Schafer, J.M., Sheng, Q., Hongo, R.A., Beckermann, K.E.,
825 Wheeler, F.C., Lehmann, B.D., and Pietenpol, J.A. (2021). Acquisition of aneuploidy drives mutant p53-associated
826 gain-of-function phenotypes. Nature communications *12*, 5184. 10.1038/s41467-021-25359-z.
827 62. Vasiliev, J.M., Gelfand, I.M., Domnina, L.V., Ivanova, O.Y., Komm, S.G., and Olshevskaja, L.V. (1970). Effect of
828 colcemid on the locomotory behaviour of fibroblasts. J Embryol Exp Morphol *24*, 625-640.

829 63. Liao, G., Nagasaki, T., and Gundersen, G.G. (1995). Low concentrations of nocodazole interfere with fibroblast
830 locomotion without significantly affecting microtubule level: implications for the role of dynamic microtubules
831 in cell locomotion. J Cell Sci *108 (Pt 11)*, 3473-3483. 10.1242/jcs.108.11.3473.
832 64. Etienne-Manneville, S. (2013). Microtubules in cell migration. Annu Rev Cell Dev Biol *29*, 471-499.
833 10.1146/annurev-cellbio-101011-155711.
834 65. Anderson, D.R., Meyers, M.J., Vernier, W.F., Mahoney, M.W., Kurumbail, R.G., Caspers, N., Poda, G.I., Schindler,
835 J.F., Reitz, D.B., and Mourey, R.J. (2007). Pyrrolopyridine inhibitors of mitogen-activated protein kinase-activated
836 protein kinase 2 (MK-2). J Med Chem *50*, 2647-2654. 10.1021/jm0611004.
837 66. Stokoe, D., Engel, K., Campbell, D.G., Cohen, P., and Gaestel, M. (1992). Identification of MAPKAP kinase 2 as a
838 major enzyme responsible for the phosphorylation of the small mammalian heat shock proteins. FEBS Lett *313*,
839 307-313. 10.1016/0014-5793(92)81216-9.
840 67. Lopes, L.B., Flynn, C., Komalavilas, P., Panitch, A., Brophy, C.M., and Seal, B.L. (2009). Inhibition of HSP27
841 phosphorylation by a cell-permeant MAPKAP Kinase 2 inhibitor. Biochem Biophys Res Commun *382*, 535-539.
842 10.1016/j.bbrc.2009.03.056.
843 68. Guo, M., Sun, D., Fan, Z., Yuan, Y., Shao, M., Hou, J., Zhu, Y., Wei, R., Zhu, Y., Qian, J., et al. (2019). Targeting MK2
844 Is a Novel Approach to Interfere in Multiple Myeloma. Front Oncol *9*, 722. 10.3389/fonc.2019.00722.
845 69. Gu, C., Cheng, H., Yang, H., Bian, Y., Wang, Y., Zhang, Y., Pisano, M., Hu, G., and Yang, Y. (2021). MK2 is a
846 therapeutic target for high-risk multiple myeloma. Haematologica *106*, 1774-1777.
847 10.3324/haematol.2017.182121.
848 70. Berggren, K.L., Restrepo Cruz, S., Hixon, M.D., Cowan, A.T., Keysar, S.B., Craig, S., James, J., Barry, M., Ozbun, M.A.,
849 Jimeno, A., et al. (2019). MAPKAPK2 (MK2) inhibition mediates radiation-induced inflammatory cytokine
850 production and tumor growth in head and neck squamous cell carcinoma. Oncogene *38*, 7329-7341.
851 10.1038/s41388-019-0945-9.
852 71. Kudaravalli, S., den Hollander, P., and Mani, S.A. (2022). Role of p38 MAP kinase in cancer stem cells and
853 metastasis. Oncogene *41*, 3177-3185. 10.1038/s41388-022-02329-3.
854 72. Morgan, D., Berggren, K.L., Spiess, C.D., Smith, H.M., Tejwani, A., Weir, S.J., Lominska, C.E., Thomas, S.M., and
855 Gan, G.N. (2022). Mitogen-activated protein kinase-activated protein kinase-2 (MK2) and its role in cell survival,
856 inflammatory signaling, and migration in promoting cancer. Mol Carcinog *61*, 173-199. 10.1002/mc.23348.
857 73. Pomerance, M., Quillard, J., Chantoux, F., Young, J., and Blondeau, J.P. (2006). High-level expression, activation,
858 and subcellular localization of p38-MAP kinase in thyroid neoplasms. J Pathol *209*, 298-306. 10.1002/path.1975.
859 74. Suresh, K., Del Rosario, O., Kallem, M., Singh, G., Shah, A., Zheng, L., Yun, X., Philip, N.M., Putcha, N., McClure,
860 M.B., et al. (2023). Tumor MK2 transcript levels are associated with improved response to chemotherapy and
861 patient survival in non-small cell lung cancer. Physiol Genomics *55*, 168-178.
862 10.1152/physiolgenomics.00155.2022.
863 75. Suzuki, A., Badger, B.L., Wan, X., DeLuca, J.G., and Salmon, E.D. (2014). The architecture of CCAN proteins creates
864 a structural integrity to resist spindle forces and achieve proper Intrakinetochore stretch. Developmental cell *30*,
865 717-730. 10.1016/j.devcel.2014.08.003
866 S1534-5807(14)00513-9 [pii].
867 76. Suzuki, A., Badger, B.L., and Salmon, E.D. (2015). A quantitative description of Ndc80 complex linkage to human
868 kinetochores. Nature Communication *6*, 8161. 10.1038/ncomms9161.

77. Chandradoss, S.D., Haagsma, A.C., Lee, Y.K., Hwang, J.H., Nam, J.M., and Joo, C. (2014). Surface passivation for single-molecule protein studies. J Vis Exp. 10.3791/50549.

78. Pinder, S.E., Ellis, I.O., Galea, M., O'Rouke, S., Blamey, R.W., and Elston, C.W. (1994). Pathological prognostic factors in breast cancer. III. Vascular invasion: relationship with recurrence and survival in a large study with long-term follow-up. Histopathology *24*, 41-47. 10.1111/j.1365-2559.1994.tb01269.x.

79. Lauria, R., Perrone, F., Carlomagno, C., De Laurentiis, M., Morabito, A., Gallo, C., Varriale, E., Pettinato, G., Panico, L., Petrella, G., et al. (1995). The prognostic value of lymphatic and blood vessel invasion in operable breast cancer. Cancer *76*, 1772-1778. 10.1002/1097-0142(19951115)76:10<1772::Aid-cncr2820761014>3.0.Co;2-o.

80. Dobin, A., Davis, C.A., Schlesinger, F., Drenkow, J., Zaleski, C., Jha, S., Batut, P., Chaisson, M., and Gingeras, T.R. (2013). STAR: ultrafast universal RNA-seq aligner. Bioinformatics *29*, 15-21. 10.1093/bioinformatics/bts635.

81. Liao, Y., Smyth, G.K., and Shi, W. (2013). featureCounts: an efficient general purpose program for assigning sequence reads to genomic features. Bioinformatics *30*, 923-930. 10.1093/bioinformatics/btt656.

82. Love, M.I., Huber, W., and Anders, S. (2014). Moderated estimation of fold change and dispersion for RNA-seq data with DESeq2. Genome Biology *15*. 10.1186/s13059-014-0550-8.

83. Huang, D.W., Sherman, B.T., and Lempicki, R.A. (2008). Systematic and integrative analysis of large gene lists using DAVID bioinformatics resources. Nature protocols *4*, 44-57. 10.1038/nprot.2008.211.

909
910
911
912
913
914
915

916 **Legends**

917 **Figure 1. CMPD1 induced severe mitotic arrest in multiple cancer cell lines**

918 (A) Chemical structure of CMPD1. (B) FACS analysis of MDA-MB-231 cells treated with
919 DMSO or 1, 5, or 10 μM CMPD1 for 24 hours. (C) Representative time-lapse images of
920 MDA-MB-231, CAL-51, and T-47D cells treated with either DMSO or 5 μM CMPD1. Time is
921 indicated in minutes post-NEBD. (D) Quantification of mitotic duration of MDA-MB-231, CAL-
922 51, and T-47D treated with DMSO, 1, 5, or 10 μM CMPD1. n = 30-60 cells pooled from two
923 independent replicates. Error bars are mean ± s.d. Asterisk above each dot plot indicates
924 the significant difference ($p < 0.0001$, Tukey's multiple comparison test) between the
925 indicated drug-treated condition and the control.

926

927 **Figure 2. CMPD1 treatment specifically attenuates mitotic fidelity of cancer cells**

928 (A) Representative time-lapse images (interval: 3 min) of RPE1, MDA-MB-231, and CAL-51
929 cells treated with DMSO or low dose of CMPD1 (10 and 50 nM). All of these three cell lines
930 express H2B-GFP. Time is indicated in minutes post-NEBD. (B) Quantification of mitotic
931 duration of cells shown in (A). n = 70, 60, 60, 60, 60, 65, 50, 84, 101 cells from left to right.

932 (C) The enlarged plot of a red box region shown in (B). (D) Representative images of mitotic
933 defects. Note that “misaligned” and “no metaphase plate” were annotated only when the
934 cells exhibited this phenotype upon anaphase onset. (E) Normalized percentage of mitotic
935 cells exhibiting accurate chromosome segregation in each condition. The data derived from
936 CMPD1-treated cells were normalized to the data derived from DMSO-treated cells for each
937 cell line. (F) Left: representative time-lapse images (interval: 3 min) of untreated RPE1 cells,
938 and RPE1, MDA-MB-231, and CAL-51 cells treated with 10 nM PTX. Right: The
939 quantification of the fraction of mitotic cells showing mitotic errors. The p-value was
940 calculated by Tukey's multiple comparisons test. Time is indicated in minutes post-washout.
941 (G) Representative images of RPE1, MDA-MB-231, and CAL-51 cells in CMPD1 washout
942 experiments. Briefly, cells were treated with 2 μM CMPD1 for 4 hours, followed by a wash
943 with complete media and live-cell imaging. Time is indicated in minutes post-washout. (H)
944 The mitotic duration of mitotic cells that were arrested by CMPD1 in the beginning of the
945 imaging. The mitotic duration was defined as the time from the start of the imaging to
946 anaphase onset or mitotic exit. The mean value was shown at the top right of each condition.
947 n = 54, 60, and 37 cells for RPE1, MDA-MB-231, and CAL-51 cells, respectively. The p-
948 value was calculated by Tukey's multiple comparisons test. (I) Quantification of the
949 percentage of mitotic cells showing normal chromosome segregation. The mean value was
950 shown at the top right of each condition. n = 50 cells in each condition pooled from two
951 independent experiments. The p-value was calculated by Tukey's multiple comparisons test.

952 Error bars are mean ± s.d.

953

954 **Figure 3. CMPD1 inhibits both anchorage independent growth and tumor growth in**

955 **mice**

956 (A) Representative images of anchorage independent growth assay using MDA-MB-231

957 cells treated with DMSO, CMPD1 at different conditions (0.01, 0.05, 0.1, 0.25, 0.5, and 1

958 μM), or 10 μM PTX. (B) The normalized number of cell colonies formed in each condition.

959 Error bars are mean ± s.d. Three independent experiments were performed for each

960 condition. (C) Schematic diagram of the mouse xenograft experiment using MDA-MB-231

961 and the drug treatment schedule. (D) The photo of tumors in each condition at the time of

962 necropsy. The tumors were arranged in order based on their size. (E) Quantification of the

963 gross weight of tumors in the mouse xenograft experiment using MDA-MB-231 cells at the

964 time of necropsy. (F) Quantification of the tumor volume during the treatment regimen in the

965 mouse xenograft experiment using CAL-51 cells. (G) Quantification of the gross weight of

966 tumors in the mouse xenograft experiment using CAL-51 cells at the time of necropsy.

967

968 **Figure 4. CMPD1 induces microtubule depolymerization**

969 (A) Representative time-lapse images of CAL-51 cells expressing α-Tubulin-mNeonGreen

970 and H2B-mScalret upon the treatment with DMSO, 2 μM CMPD1, or 10 μM MG132 along

971 with 2 μM CMPD1. CMPD1 was added into the cell culture media immediately after images

972 at the first time point were acquired. Time is indicated in minutes. (B) The quantification of
973 the signal levels of mitotic spindles over time in each condition shown in (A). (C)
974 Representative time-lapse images (interval: 2 min) of a G2 phase CAL-51 cell expressing α-
975 Tubulin-mNeonGreen and H2B-mScarlet in the presence of 2 μM CMPD1. Note that the two
976 bright dots in the Tubulin channel indicate the two clustered centrosomes before NEBD. The
977 arrow in the DNA channel indicates the time of NEBD. Time is indicated in minutes. (D)
978 Representative kymographs depicting microtubule plus and minus end dynamics before and
979 after the addition of polymerization mix supplement with 15 μM tubulin alone, or 15 μM
980 tubulin supplemented with either 20 μM CMPD1 or 5 μM vinblastine, as indicated
981 (GMPCPP-stabilized microtubule seeds, magenta; microtubules polymerized from seeds,
982 green; see Methods). Plus ends are positioned to the right, and minus ends are positioned
983 to the left of the seeds in all kymographs. Red arrow and dashed line indicate the time of
984 addition of tubulin alone, or tubulin plus drug. (E) Plot depicting fraction of microtubules with
985 detectable plus or minus ends 1 minute after addition of drug, or tubulin alone (n = 27, 29,
986 and 30 microtubules from left to right). Error bars indicate mean ± s.d. (F) Representative
987 images from a time-lapse sequence showing microtubule plus and minus end lengths 10
988 seconds prior to, and 5 and 15 seconds after addition of polymerization mix supplemented
989 with 20 μM CMPD1. (G) Plots depicting plus end catastrophe frequencies (n = 51 and 41
990 microtubules from left to right), plus end growth rates (n = 172 and 91 events from left to
991 right), and normalized maximum length (n = 55 and 41 microtubules from left to right)

992 achieved over the imaging period. (H) Plots depicting minus end catastrophe frequencies (n
993 = 51 and 41 microtubules from left to right), minus end growth rates (n = 129 and 63 events
994 from left to right), and normalized maximum length (n = 55 and 40 microtubules from left to
995 right) achieved over the imaging period. Error bars indicate mean ± s.d. Data were pooled
996 from at least 2-4 independent replicates (G-H).
997
998 **Figure 5. CMPD1 inhibits cancer cell migration and invasion**
999 (A) Representative images of H2B-mScarlet CAL-51 cells treated with DMSO, or CMPD1 at
1000 different concentrations (0, 0.1, 0.5, 1, 10 μM) at three different time points (0, 24, and 48 hr
1001 post-treatment). A wound (cell-free zone) was created using a tip, followed by the addition
1002 of indicated drugs and live-cell imaging (interval: 30 min). (B) Quantification of cell migration
1003 speed when cells were treated with indicated drugs. Each condition was normalized to the
1004 speed of DMSO-treated cells. The distance between the edge of the wound was measured
1005 using imageJ macro. Results are the mean ± s.d. N = 3 biological replicates. (C)
1006 Representative images of trans-well invasion assay using MDA-MB-231 cells treated with
1007 DMSO, CMPD1 (0.1, 1, 2, 5 μM), or 10 μM PTX. (D) The quantification of the average
1008 number of invaded cells in each condition shown in (C). (E) Left: example images of blood
1009 vessels in xenograft tumors derived from mice treated with DMSO or 1.0 mg/kg CMPD1 as
1010 shown in Fig. 3C. Two sets of example images acquired from different tumors were shown.
1011 Right: the quantification of the percentage of blood vessels infiltrated with cancer cells. Error

1012 bars are mean ± s.d.

1013

1014 **Figure 6. MK2 inhibition enhances the efficacy of microtubule inhibitors in cancer**

1015 **cells**

1016 (A) Left: representative time-lapse images of mitotic CAL-51 cells treated with indicated

1017 combinations of drugs (10 μM MK2i, 1 nM vinblastine, 5 nM vinblastine). Right: quantification

1018 of the mitotic duration, mitotic error rate, mitotic slippage rate, and the frequency of death in

1019 mitosis. The fate of mitotic cells was color-coded as indicated above the quantification plots.

1020 N = 100 cells pooled from two biological replicates for each condition. Time shown on the

1021 upper right corner of the representative images is indicated in minutes after NEBD. (B)

1022 Volcano plot displaying changes in gene expression following CMPD1 treatment in MDA-

1023 MB-231 cells. RNA-seq was conducted with three biological replicates. Differentially

1024 expressed genes (DEGs) are highlighted in red (up-regulated) and blue (down-regulated).

1025 (C) Pathway enrichment analysis of differentially expressed genes using the Gene Ontology

1026 (GO) Biological Processes (BP). Enrichment analysis was performed with the DAVID online

1027 tool. (D) Comparison of GO Biological Process enrichment analysis of DEGs unique to MDA-

1028 MB-231 cells relative to RPE1 cells. Genes uniquely up- or down-regulated in MDA-MB-231

1029 cells, but not in RPE1 cells, were subjected to GO BP enrichment analysis.

1030

1031 **Figure 7. The model of CMPD1-mediated cytotoxicity effects on cancer cells.**

1032 CMPD1 exhibits its tumor-specific cytotoxicity likely via two pathways. First, CMPD1 acts as
1033 a kinase inhibitor which prevents p38 MAPK-dependent phosphorylation of MK2, leading to
1034 the disruption of proper actin remodeling and spindle formation during mitosis. Second,
1035 CMPD1 serves as a MTA which can specifically induce depolymerization at the plus ends of
1036 microtubules. Both impaired actin reorganization and attenuated microtubule filament
1037 formation inhibit cancer cell migration and invasion, thereby preventing metastasis. On the
1038 other hand, failure of spindle assembly during mitosis causes the extended prometaphase
1039 arrest and the diminished mitotic fidelity, resulting in apoptosis of tumor cells and tumor
1040 shrinkage.
1041

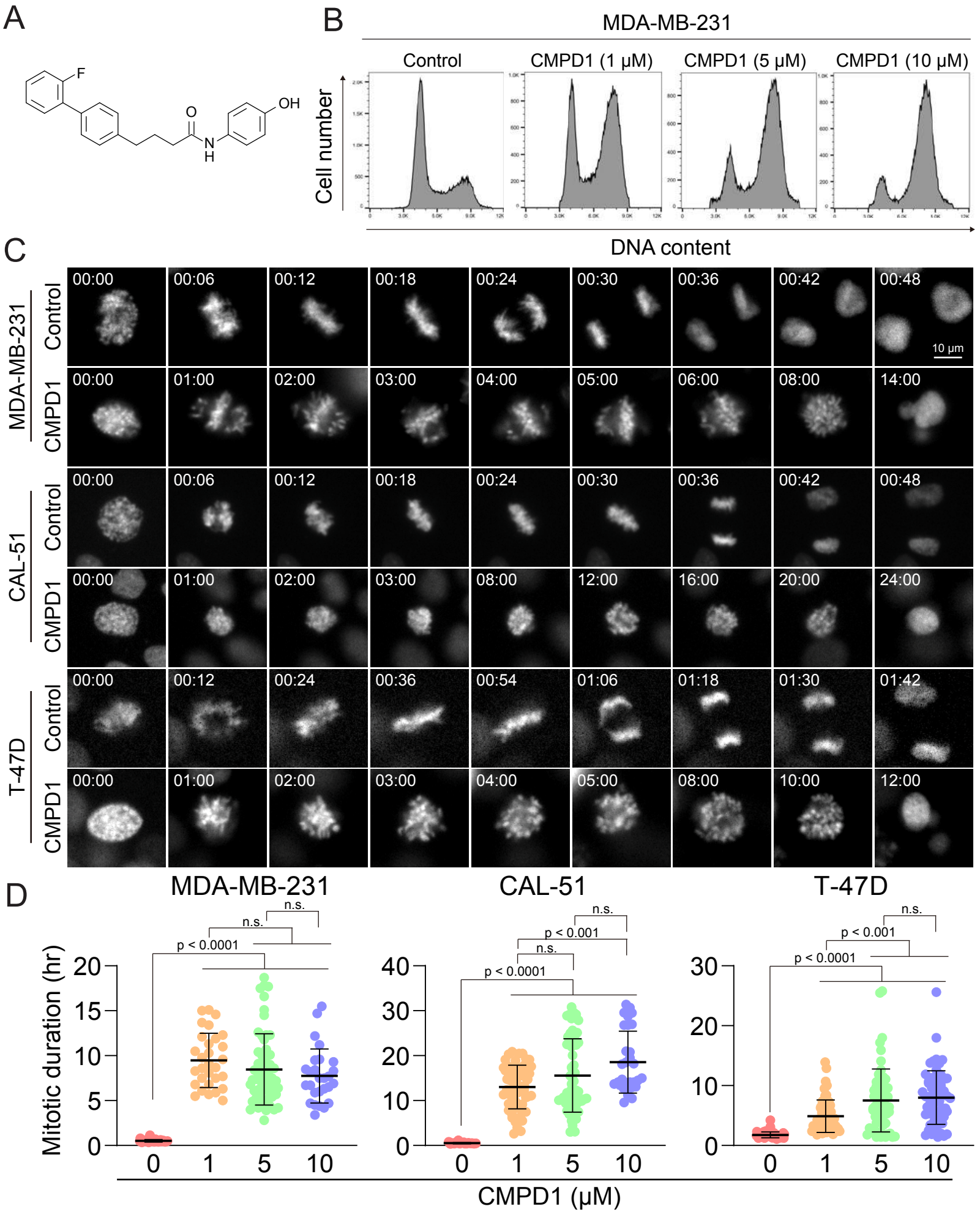
A
F
O
OH
N
H
B
MDA-MB-231
Control
CMPD1 (1 μM)
CMPD1 (5 μM)
CMPD1 (10 μM)
Cell number
DNA content
C
MDA-MB-231
Control
CMPD1
CAL-51
T-47D
10 μm
D
MDA-MB-231
CAL-51
T-47D
Mitotic duration (hr)
n.s.
p < 0.0001
p < 0.001
CMPD1 (μM)

Figure 1

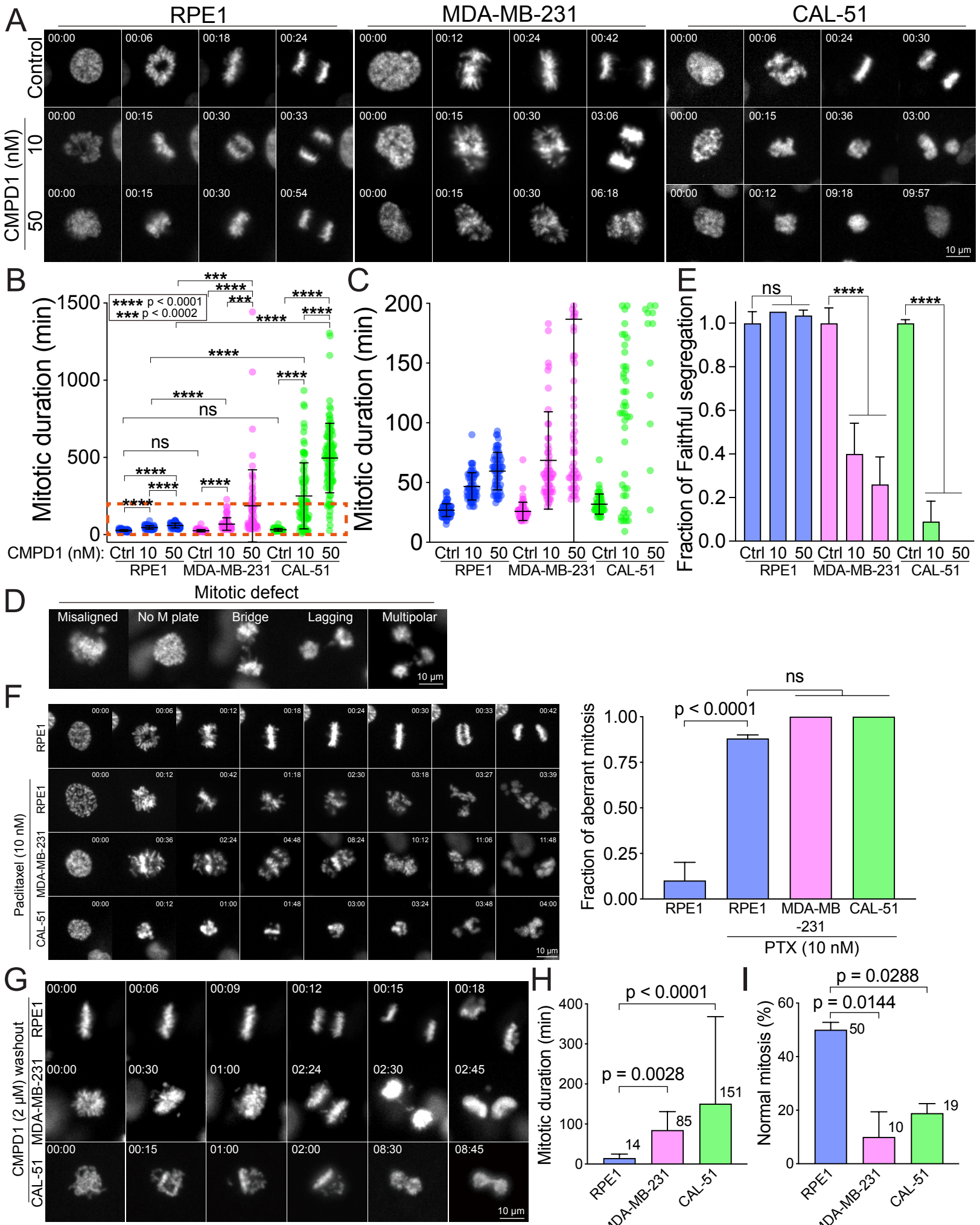
A
RPE1
MDA-MB-231
CAL-51
Control
CMPD1 (nM)
10
50
10 µm
B
Mitotic duration (min)
**** p < 0.0001
*** p < 0.0002
ns
CMPD1 (nM): Ctrl 10 50 Ctrl 10 50 Ctrl 10 50
RPE1 MDA-MB-231 CAL-51
C
Mitotic duration (min)
Ctrl 10 50 Ctrl 10 50 Ctrl 10 50
RPE1 MDA-MB-231 CAL-51
E
Fraction of Faithful segregation
ns
****
Ctrl 10 50 Ctrl 10 50 Ctrl 10 50
RPE1 MDA-MB-231 CAL-51
D
Mitotic defect
Misaligned
No M plate
Bridge
Lagging
Multipolar
10 µm
F
Paclitaxel (10 nM)
RPE1
MDA-MB-231
CAL-51
10 µm
Fraction of aberrant mitosis
ns
p < 0.0001
RPE1
RPE1
MDA-MB -231
CAL-51
PTX (10 nM)
G
CMPD1 (2 µM) washout
RPE1
MDA-MB-231
CAL-51
10 µm
H
Mitotic duration (min)
p < 0.0001
p = 0.0028
14
85
151
RPE1
MDA-MB-231
CAL-51
I
Normal mitosis (%)
p = 0.0288
p = 0.0144
50
10
19
RPE1
MDA-MB-231
CAL-51

Figure 2

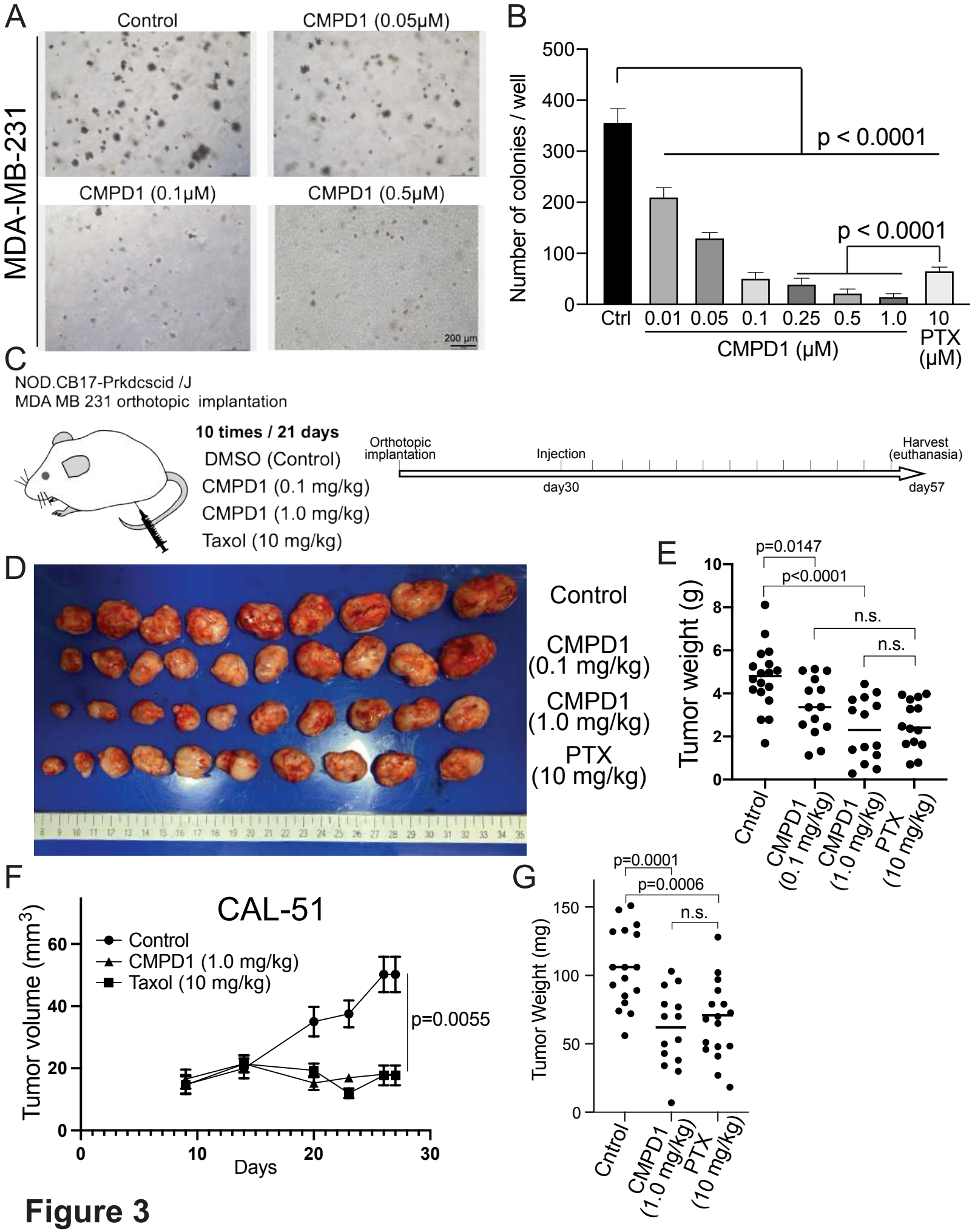
A
Control
CMPD1 (0.05μM)
CMPD1 (0.1μM)
CMPD1 (0.5μM)
MDA-MB-231
200 μm
B
Number of colonies / well
500
400
300
200
100
0
p < 0.0001
p < 0.0001
Ctrl
0.01
0.05
0.1
0.25
0.5
1.0
10
PTX (μM)
CMPD1 (μM)
C
NOD.CB17-Prkdcscid /J
MDA MB 231 orthotopic implantation
10 times / 21 days
DMSO (Control)
CMPD1 (0.1 mg/kg)
CMPD1 (1.0 mg/kg)
Taxol (10 mg/kg)
Orthotopic implantation
Injection
Harvest (euthanasia)
day30
day57
D
Control
CMPD1 (0.1 mg/kg)
CMPD1 (1.0 mg/kg)
PTX (10 mg/kg)
E
Tumor weight (g)
p=0.0147
p<0.0001
n.s.
n.s.
Cntrol
CMPD1 (0.1 mg/kg)
CMPD1 (1.0 mg/kg)
PTX (10 mg/kg)
F
CAL-51
Tumor volume (mm3)
Control
CMPD1 (1.0 mg/kg)
Taxol (10 mg/kg)
p=0.0055
Days
G
Tumor Weight (mg)
p=0.0001
p=0.0006
n.s.
Cntrol
CMPD1 (1.0 mg/kg)
PTX (10 mg/kg)

Figure 3

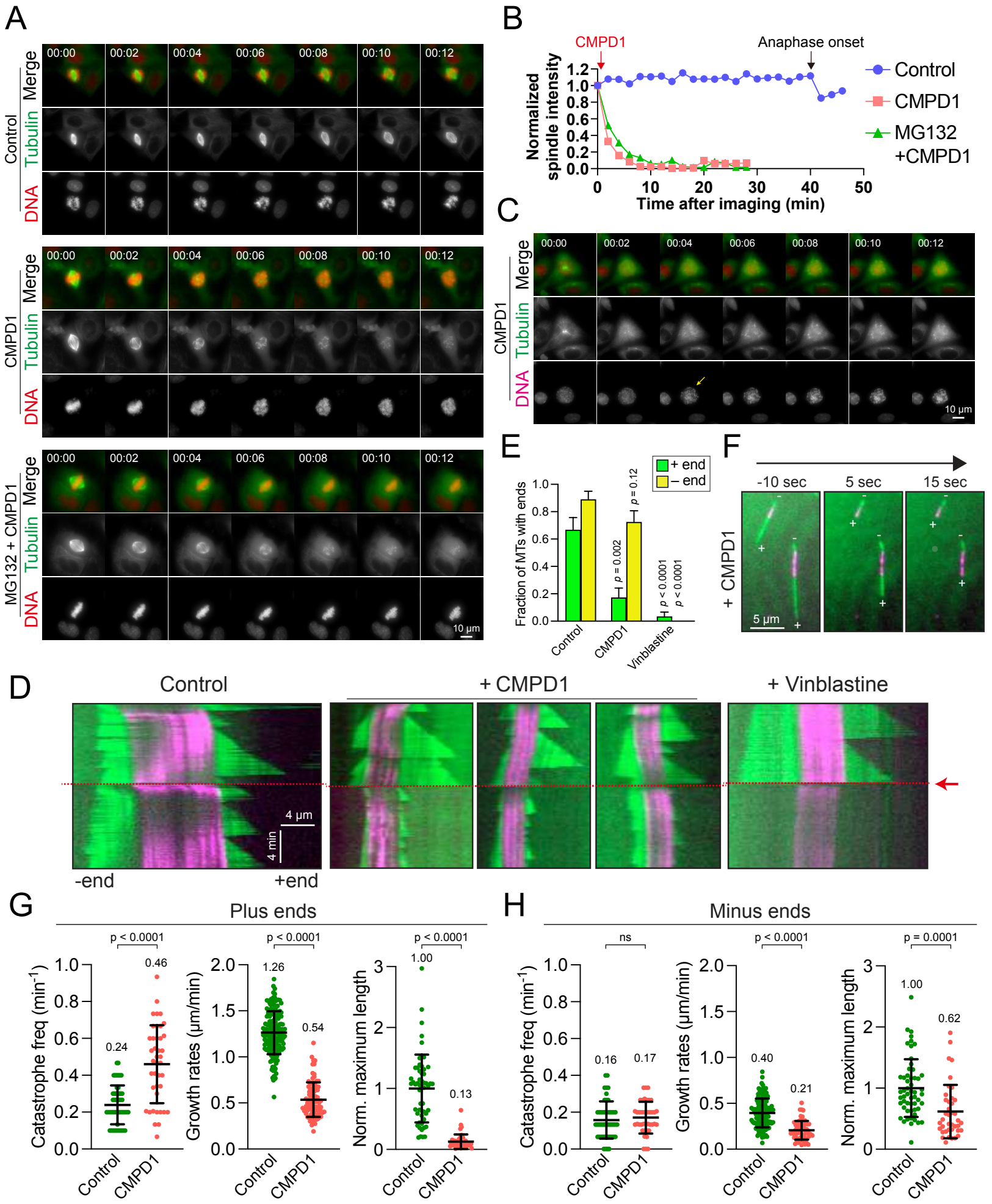
A
Control
CMPD1
MG132 + CMPD1
Merge
Tubulin
DNA
00:00
00:02
00:04
00:06
00:08
00:10
00:12
10 µm
B
CMPD1
Anaphase onset
Normalized spindle intensity
Time after imaging (min)
Control
CMPD1
MG132 +CMPD1
C
D
Control
+ CMPD1
+ Vinblastine
4 µm
4 min
-end
+end
E
Fraction of MTs with ends
+ end
– end
p = 0.002
p = 0.12
p < 0.0001
p < 0.0001
Control
CMPD1
Vinblastine
F
-10 sec
5 sec
15 sec
+ CMPD1
5 µm
G
Plus ends
p < 0.0001
Catastrophe freq (min⁻¹)
0.24
0.46
Growth rates (µm/min)
1.26
0.54
Norm. maximum length
1.00
0.13
Control
CMPD1
H
Minus ends
ns
p < 0.0001
p = 0.0001
0.16
0.17
0.40
0.21
1.00
0.62

Figure 4

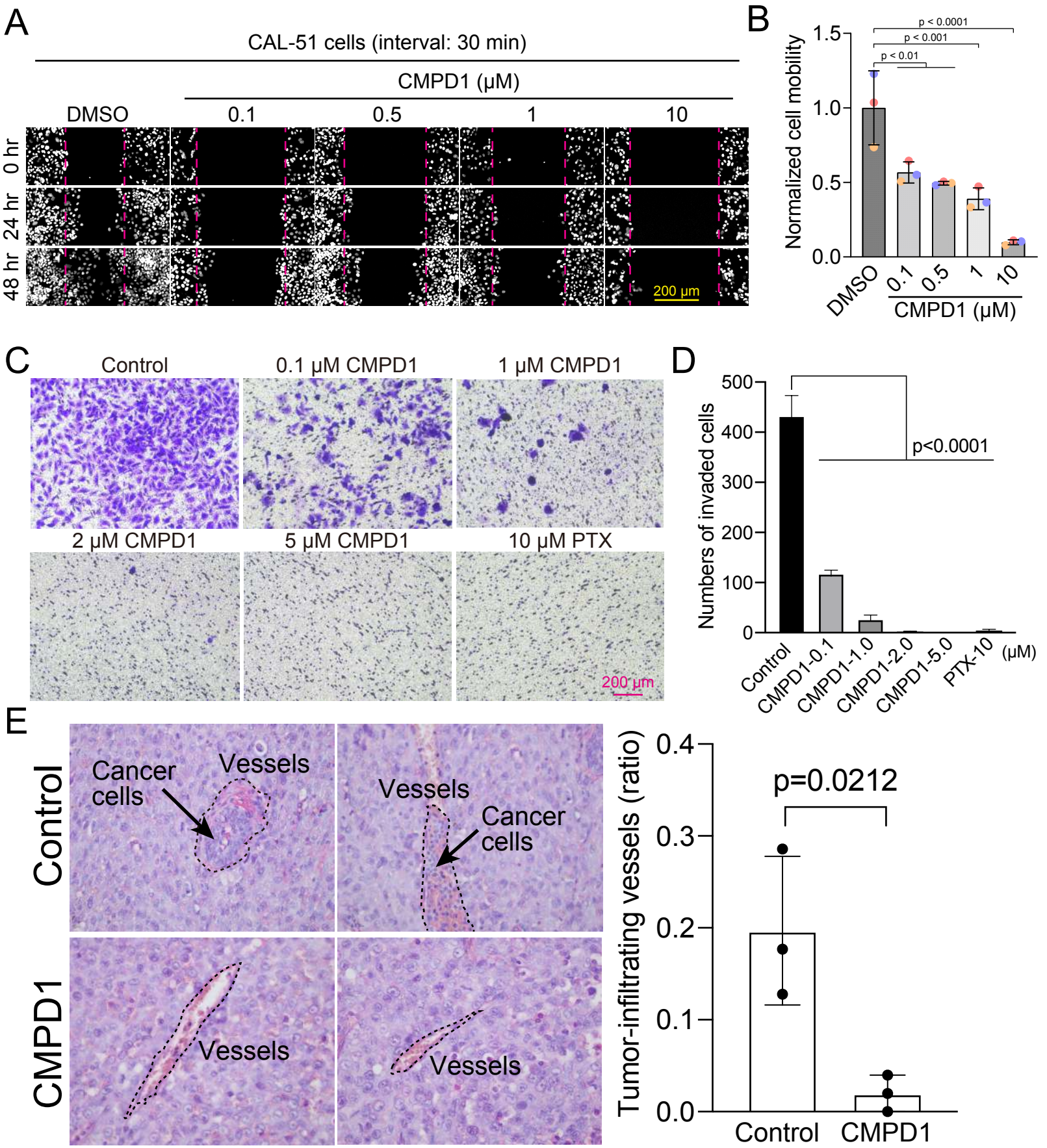
A
CAL-51 cells (interval: 30 min)
CMPD1 (μM)
DMSO
0.1
0.5
1
10
0 hr
24 hr
48 hr
200 μm
B
Normalized cell mobility
p < 0.0001
p < 0.001
p < 0.01
1.5
1.0
0.5
0.0
DMSO
0.1
0.5
1
10
CMPD1 (μM)
C
Control
0.1 μM CMPD1
1 μM CMPD1
2 μM CMPD1
5 μM CMPD1
10 μM PTX
200 μm
D
Numbers of invaded cells
500
400
300
200
100
0
p<0.0001
Control
CMPD1-0.1
CMPD1-1.0
CMPD1-2.0
CMPD1-5.0
PTX-10
(μM)
E
Control
CMPD1
Cancer cells
Vessels
Vessels
Cancer cells
Vessels
Vessels
Tumor-infiltrating vessels (ratio)
0.4
0.3
0.2
0.1
0.0
p=0.0212
Control
CMPD1

Figure 5

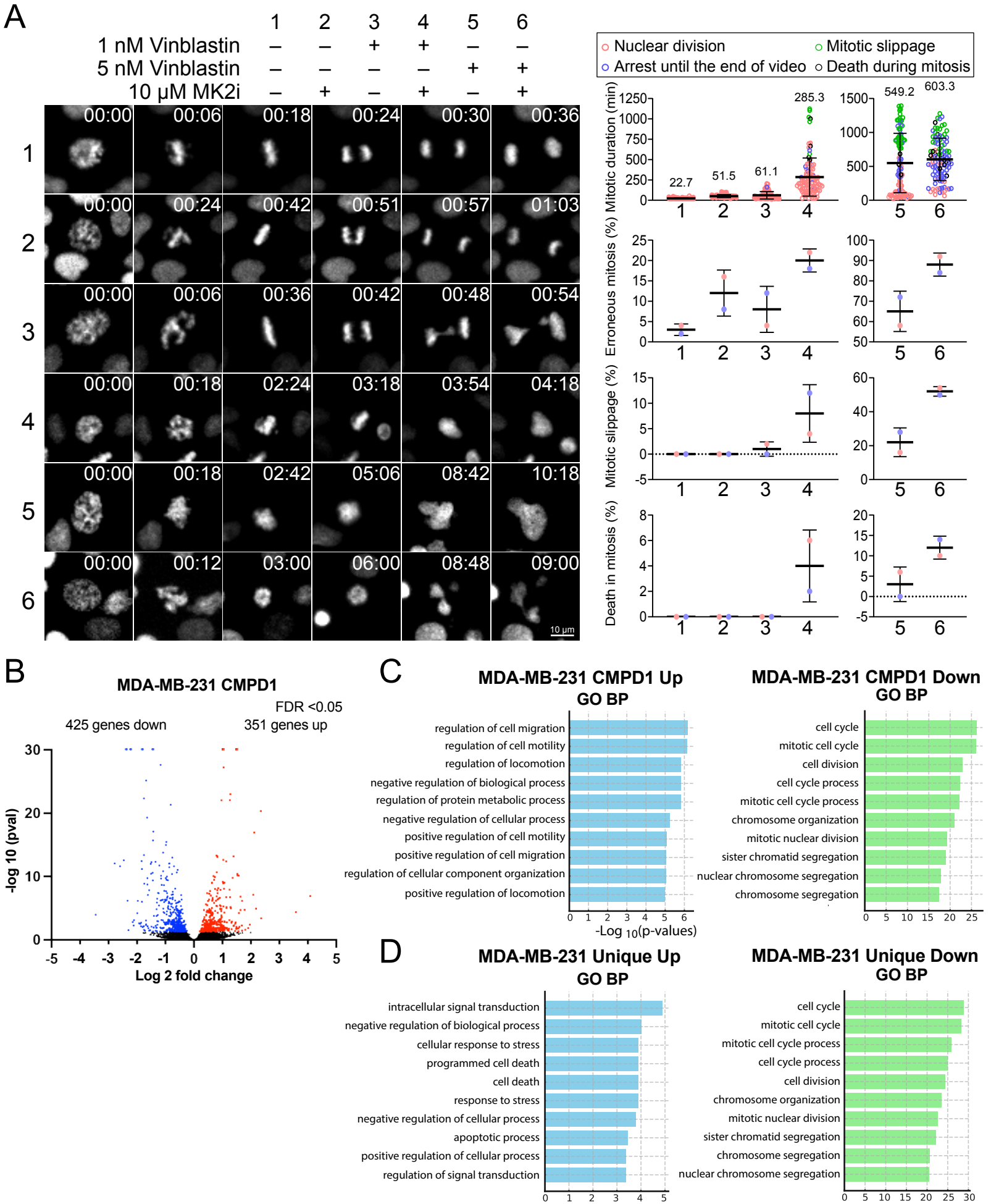
A
1 2 3 4 5 6
1 nM Vinblastin – – + + – –
5 nM Vinblastin – – – – + +
10 μM MK2i – + – + – +
00:00 00:06 00:18 00:24 00:30 00:36
00:00 00:24 00:42 00:51 00:57 01:03
00:00 00:06 00:36 00:42 00:48 00:54
00:00 00:18 02:24 03:18 03:54 04:18
00:00 00:18 02:42 05:06 08:42 10:18
00:00 00:12 03:00 06:00 08:48 09:00
10 μm
Nuclear division
Mitotic slippage
Arrest until the end of video
Death during mitosis
Mitotic duration (min)
22.7
51.5
61.1
285.3
549.2
603.3
Erroneous mitosis (%)
Mitotic slippage (%)
Death in mitosis (%)
B
MDA-MB-231 CMPD1
FDR <0.05
425 genes down
351 genes up
-log 10 (pval)
Log 2 fold change
C
MDA-MB-231 CMPD1 Up
GO BP
regulation of cell migration
regulation of cell motility
regulation of locomotion
negative regulation of biological process
regulation of protein metabolic process
negative regulation of cellular process
positive regulation of cell motility
positive regulation of cell migration
regulation of cellular component organization
positive regulation of locomotion
-Log 10(p-values)
MDA-MB-231 CMPD1 Down
GO BP
cell cycle
mitotic cell cycle
cell division
cell cycle process
mitotic cell cycle process
chromosome organization
mitotic nuclear division
sister chromatid segregation
nuclear chromosome segregation
chromosome segregation
D
MDA-MB-231 Unique Up
GO BP
intracellular signal transduction
negative regulation of biological process
cellular response to stress
programmed cell death
cell death
response to stress
negative regulation of cellular process
apoptotic process
positive regulation of cellular process
regulation of signal transduction
MDA-MB-231 Unique Down
GO BP
cell cycle
mitotic cell cycle
mitotic cell cycle process
cell cycle process
cell division
chromosome organization
mitotic nuclear division
sister chromatid segregation
chromosome segregation
nuclear chromosome segregation

Figure 6

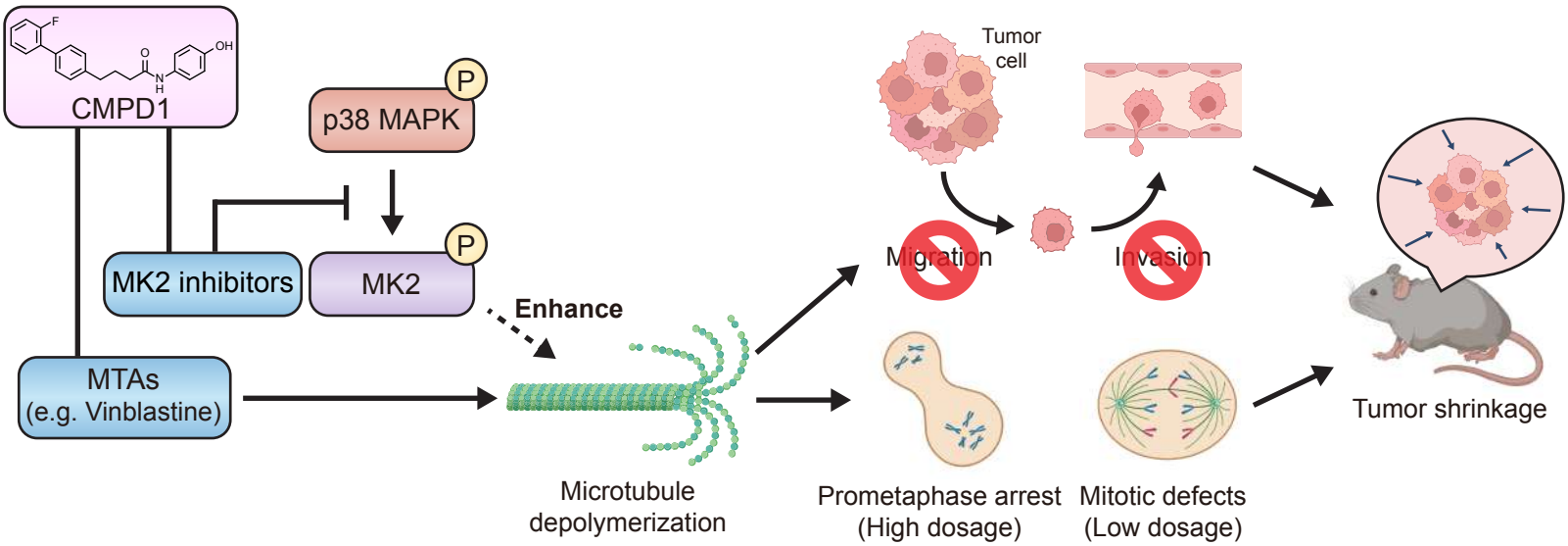
CMPD1
p38 MAPK
P
MK2 inhibitors
MK2
P
Enhance
MTAs
(e.g. Vinblastine)
Microtubule
depolymerization
Tumor
cell
Migration
Invasion
Prometaphase arrest
(High dosage)
Mitotic defects
(Low dosage)
Tumor shrinkage

Figure 7